



# Ethanol electro-oxidation on the PdSn-TaN/C catalyst in alkaline media: Making TaN capable of splitting C—C bond

Na Ye<sup>a,1</sup>, Pengcheng Zhao<sup>b,1</sup>, Xiaoying Qi<sup>a</sup>, Wenchao Sheng<sup>b</sup>, Zhao Jiang<sup>a,\*</sup>, Tao Fang<sup>a</sup>

<sup>a</sup> Department of Chemical Engineering, Shaanxi Key Laboratory of Energy Chemical Process Intensification, Engineering Research Center of New Energy System Engineering and Equipment, Xi'an Jiaotong University, Xi'an 710049, China

<sup>b</sup> College of Environmental Science and Engineering, Tongji University, 1239 Siping Road, Shanghai 200092, China

## ARTICLE INFO

### Keywords:

PdSn-TaN/C

Ethanol oxidation reactions

In situ ATR-SEIRAS (Attenuated total reflection-surface enhanced infrared absorption spectroscopy)

DFT (Density Functional Theory)

Electronic structure

## ABSTRACT

The C—C bond cleavage remains a main challenge for alkaline EOR (ethanol oxidation reaction). In this work, we report an efficient PdSn-TaN/C electrocatalyst to split the C—C bonds in ethanol. Structurally, a series of characterization results confirm the presence of the low-coordinated Pd sites on the PdSn-TaN/C interface. The PdSn-TaN/C catalyst exhibits very high activity (almost 26.9 times of commercial Pd/C), good durability and high selectivity to CO<sub>2</sub> (20.5%) towards alkaline EOR. Specifically, in-situ ATR-SEIRAS (Attenuated total reflection-surface enhanced infrared absorption spectroscopy) results indicate that TaN facilitates the cleavage of C—C bonds, whereas Sn promotes the further oxidation of ethanol fragments. DFT (density functional theory) calculations indicate the activation barriers of the C—H bond cleavage in CH<sub>3</sub>CH<sub>2</sub>OH, CH<sub>3</sub>CHOH, CH<sub>3</sub>CHO, CH<sub>3</sub>CO, CH<sub>2</sub>CO and the C—C bond cleavage in CH<sub>3</sub>CO, CH<sub>2</sub>CO, CHCO are reduced evidently and the removal of adsorbed CH<sub>3</sub>CO and CO becomes easier on the PdSn-TaN/C catalyst surface.

## 1. Introduction

Direct ethanol fuel cells (DEFCs) are attracting more and more attention as energy conversion devices because of lots of merits, including high energy density (8 kWh·kg<sup>-1</sup>), renewability and non-toxicity [1–7]. Compared with the acidic DEFCs, alkaline DEFCs has many advantages, such as the accelerated ORR (oxygen reduction reaction) reaction kinetics, the expanded catalyst ranges including non-noble catalysts [4,8–10]. Recently, the development of alkaline anion-exchange membrane further attracts more interests in the alkaline DEFCs [4,11–13]. However, the development of the alkaline DEFCs is mainly hindered by the lower oxidation efficiency and sluggish ethanol oxidation reaction (EOR) kinetics [2,14]. Specifically, for EOR, the splitting of C—C bonds to form the complete products of CO<sub>2</sub> is rather difficult, which decreases the energy utilization efficiency [7,15–18]. At the same time, the generated intermediates, such as CO and CH<sub>x</sub>, are strongly adsorbed on the catalyst surfaces and significantly slows down the reaction kinetics [7,15,19–21].

Compared to Pt, Pd-based catalyst has been considered as the effective materials for alkaline EOR to improve catalytic performance, even though Pd is not very active for acidic EOR (ethanol oxidation

reactions) [4,6]. In addition, Pd also has more abundance and lower cost than Pt, leading to that Pd may be the optional substitution for Pt for alkaline EOR [11,22]. However, regarding most of the Pd and Pt-based catalysts, it is reported that the selectivity for CO<sub>2</sub> formation is only below 10% based on the spectroscopic results, which can be due to the sluggish and inefficient oxidation kinetics [5,7,22–24]. To solve these problems, much efforts have been spent [25]. In 2009, Adzic et al. [25] had proved the successful cleavage of C—C bonds on Pt/Rh/SnO<sub>2</sub> for acidic EOR, in which the presence of Rh was responsible for the effective splitting of C—C bonds. In 2013, they [26] indicated that high-content Ir modification could effectively cleave the C—C bonds for acidic EOR. However, both Rh and Ir are not only the noble metals but their abundances are scarce, which inhibited their practical applications [15,17,19,23,25,27]. Furthermore, in addition to the C—C bond cleavage, the dissociation of the strongly adsorbed ethanol fragments is also an obstacle [6,16]. Therefore, there is an urgent need to explore the high-efficient Pd-based catalysts with low cost to cleave the C—C bonds and accelerate the oxidation of intermediates towards alkaline EOR. In addition, it is also necessary to clarify the possible reaction mechanism for alkaline EOR to provide a reference for the design of efficient electrocatalysts.

\* Corresponding author.

E-mail address: [jiangzhao@mail.xjtu.edu.cn](mailto:jiangzhao@mail.xjtu.edu.cn) (Z. Jiang).

<sup>1</sup> These authors contributed equally to this work and should be regarded as co-first authors.

As is known to us, the catalytic performance is always sensitive to the surface structure and composition of catalysts, thus the surface engineering is expected to address these problems [2,15,18,20,23,28]. Tantalum nitride (TaN) exhibits Pt-like electronic structures, good chemical stability and low cost, which may be as the promising catalysts in the electrochemical applications. Previous reports have indicated that the interaction between TaN and other co-catalysts can lead to the improvement of the cathodic ORR performance and solar water oxidation [29–31]. To our knowledge, there is few investigation on TaN-based catalysts for the electro-oxidation of ethanol, especially for the capacity to cleave the C—C bonds. Our groups have previously reported the synthesis of Pd-TaN/C (Pd of 3.33 wt%) for alkaline MOR (methanol oxidation reaction), which can offer more interfacial active sites and enhance the MOR performance [32]. The results indicate that TaN is a promising inexpensive dopant that can improve the catalytic performance and reduce the noble metal loading. Furthermore, doping with the oxophilic elements (i.g. Sn) has been demonstrated to be an effective method to facilitate the removal of the intermediates by forming large amounts of OH that reacts with the intermediates [10,19,33]. Based on this, coupling the two substances in a reasonable way is expected to significantly enhance the selectivity of CO<sub>2</sub> and reaction kinetics for alkaline EOR on Pd-based catalysts.

According to the above analysis, in this work, we report the preparation of PdSn-TaN/C catalyst via a mild solvothermal approach. At the same time, a new enhancement mechanism of alkaline EOR is put forward and proved for the first time, that is, TaN give a preference of C—C bonds cleavage for complete oxidation of alkaline ethanol to CO<sub>2</sub>, and Sn modification contributes to the formation of the OH and thus promotes the further oxidation of ethanol fragments. Specifically, a series of structural characterization are performed to identify the compositions and surface structure. The direct spectroscopic evidences provided by the in situ attenuated total reflection-surface enhanced infrared absorption spectroscopy (ATR-SEIRAS) results are also shown to identify the reaction intermediates and understand the corresponding reaction mechanism fundamentally. DFT (density functional theory) calculations are further employed to provide evidence of the possibly involved reaction intermediates and mechanism at the atomic level. The combination of electrochemical results and in situ ATR-SEIRAS results prove that the optimized PdSn-TaN/C catalyst displays the superior activity for alkaline EOR and good selectivity to CO<sub>2</sub> by splitting C—C bonds. Overall, the work may offer a mechanism to understand how the inexpensive TaN-based catalysts to enhance catalytic performance for liquid fuels, and also extends the electrochemical applications of transition metal nitrides.

## 2. Experimental

### 2.1. Chemicals

Cabot carbon black (VXC-72R), commercial Pd/C catalyst (10% on carbon; Alfa Aesar), Na<sub>2</sub>PdCl<sub>4</sub> (≥ 99.9%; Aladdin), SnCl<sub>2</sub>·2H<sub>2</sub>O (≥ 99%; Aladdin), TaN (≥ 99.5%; Aladdin), KOH (≥ 85%; Aladdin), sodium citrate dihydrate (AR; Sinopharm Chemical Reagent Co. Ltd.), ethylene glycol (EG, AR; Sinopharm Chemical Reagent Co. Ltd.), ethanol (AR; Sinopharm Chemical Reagent Co. Ltd.) and H<sub>2</sub>SO<sub>4</sub> (≥ 98%; Sinopharm Chemical Reagent Co. Ltd.) were used as received with no further purification. Ultrapure water (18.2 MΩ·cm) was utilized in this work.

### 2.2. Catalysts preparation

The preparation procedure of Pd<sub>1</sub>Sn<sub>3</sub>-TaN/C was as follows: 135 mg TaN and 67.5 mg VXC-72R carbon were added to 33.75 mL EG, and ultrasonically dispersed. Then, 50 mg of sodium citrate dihydrate, 1 mL of KOH solution (1 M), 260 μL of Na<sub>2</sub>PdCl<sub>4</sub> (19 g·L<sup>-1</sup>) and 2 mL of SnCl<sub>2</sub>·2H<sub>2</sub>O (5 g·L<sup>-1</sup>, the solvent was EG) were added to 8 mL of the above solution (the Pd loading was 2.86 wt%). Subsequently, the mixed

solution was taken to heat to 393 K and maintained for five hours. Finally, after cooled to room temperature, it was washed centrifugally for 3 times with water and ethanol, and dried overnight at 333 K in a vacuum oven to collect the Pd<sub>1</sub>Sn<sub>3</sub>-TaN/C catalyst. The preparation processes of the Pd-TaN/C and PdSn/C catalysts were similar to the above method except the absence of the Sn and TaN. The actual loading amounts of these catalysts were measured by ICP-MS, which are shown in Table S1 (Supporting information).

### 2.3. Material characterizations

X-ray diffraction (XRD) was carried out on D8 Advance diffractometer (Bruker) using Cu Kα radiation (λ = 1.5406 Å) at 40 kV and 40 mA to study the crystalline structure. The inductively coupled plasma-mass spectroscopy (ICP-MS) equipped with a NexION 350D spectrometer was employed to identify the metal weight percentage. Transmission electron microscopy (TEM), high-resolution TEM (HRTEM) and EDS (Energy-dispersive X-ray spectroscopy) mapping were conducted on Talos F200 operated at 200 kV to further probe the nanostructure and morphology. To explore the properties and variance in electronic structure, XPS spectra were recorded on a Thermo Fisher ESCALAB Xi+ spectrometer (XPS) with a monochromatic Al Kα X-ray source (1486.6 eV) and an operating power of 400 W. Raman spectroscopy was carried out on a LabRAM HR Evolution Raman spectrometer (Horiba) with a laser wavelength of 532 nm to further investigate the composition and microstructure. Diffuse reflectance infrared Fourier transform spectroscopy (DRIFTS) was conducted on the Nicolet iS50 spectrometer. For the CO DRIFTS measurements, the samples were kept in a Ar flow (20 mL/min) for 5 min, and then recorded as a background spectrum. Subsequently, CO was passed over the samples (20 mL/min). After the CO signals were stable, spectra were collected in the range 4000–650 cm<sup>-1</sup> with 64 accumulation scans at room temperature and a resolution of 4 cm<sup>-1</sup>.

### 2.4. In situ ATR-SEIRAS measurements

In situ attenuated total reflection-surface enhanced infrared absorption spectroscopy (ATR-SEIRAS) was performed in the work to gain insight into the EOR mechanism. Detailed preparation procedures were on base of the previous literature and shown in Supporting Information (SI) [34–36].

### 2.5. Electrochemical measurements

All electrochemical tests were performed on a CHI 650B electrochemical workstation. The reference electrode adopted an Ag/AgCl electrode. A Pt wire was served as the counter electrode. Typically, 4 mg of catalysts and 30 μL of the Nafion (5%) were mixed in a solution including 500 μL of ultrapure water and 500 μL of isopropanol, and then ultrasonicated for 3 h. After that, 10 μL of the ink mixture was dropped on a polished glassy-carbon electrode (5 mm) and then dried to serve as the working electrode. Initially, all the electrolytes have to be bubbled by Ar for 20 min to remove the dissolved oxygen. Additionally, each working electrode was activated in a KOH solution by scanning between 0 and 1.2 V vs RHE at a sweep rate of 50 mV/s until the CV curve stayed unchanged. Detailed CO stripping procedures were shown in Supporting Information (SI).

### 2.6. DFT calculations

Density functional theory (DFT) calculations were performed using the Vienna Ab-initio Simulation Package (VASP) [37]. The projector augmented wave (PAW) method and Perdew - Burke - Emzerhof (PBE) functional were applied to describe the electron-ion interaction and exchange-correlation energies for all the systems. A kinetic cutoff energy of 400 eV were utilized for structure optimization and transition state

(TS) calculations. A  $3 \times 3 \times 1$  k-points was set for the Brillouin-zone integration [38]. The energy convergence criterion was  $1 \times 10^{-5}$  eV. Similar to our previous work [32,39,40], the different models were employed. For the Pd(111) surface, a  $4 \times 4$  super-cell with four-layers was used. The Pd<sub>4</sub>/TaN(001) surface was formed by depositing the Pd<sub>4</sub> cluster on TaN(001), which presented the Pd-TaN/C catalyst and was in accordance with the previous study [32]. The PdSn-TaN/C catalyst was modeled using the Pd<sub>4</sub>-SnO<sub>2</sub>/TaN(001) surface, which is anchored by the co-adsorbed Pd<sub>4</sub> and SnO<sub>2</sub> clusters on TaN(001). For Pd<sub>4</sub>/TaN(001) and Pd<sub>4</sub>-SnO<sub>2</sub>/TaN(001), a  $2 \times 4$  super-cell with four layers was used and shown in Fig. S1. The transition states were optimized and identified using the climbing images nudged elastic band (CI-NEB) algorithm. The adsorption energy  $E_{\text{ads}}$  was calculated as follows:

$$E_{\text{ads}} = E_{\text{adsorbate+surface}} - (E_{\text{adsorbate}} + E_{\text{surface}}) \quad (1)$$

where  $E_{\text{adsorbate+surface}}$  is total energy of surface covered with adsorbates,  $E_{\text{surface}}$  and  $E_{\text{adsorbate}}$  are the energies of optimized clean surface and isolated adsorbate, respectively.

### 3. Results and discussion

#### 3.1. Characterization of the PdSn-TaN/C, Pd-TaN/C and PdSn/C catalysts

The PdSn-TaN/C catalyst is prepared by the mild solvothermal method in ethylene glycol with the absence of the surfactant, similar to previous synthesis [32]. To better reveal the effects of Sn and nitride, Pd-TaN/C and PdSn/C are also prepared by the similar method. The ICP-MS results in Table S1 indicate that the actual loading of these catalysts is close to the addition amount, suggesting that the preparation is suitable for these catalysts. Additionally, the commercial Pd/C catalyst is also chosen as a reference.

To investigate the crystal structures of the mentioned catalysts, Fig. 1 presents the XRD patterns. With respect to PdSn-TaN/C and Pd-TaN/C catalysts, the sharp and intense diffraction peaks (labeled by \* and  $\triangle$ ) corresponding to the TaN and TaN<sub>0.8</sub> indicate the existence of good crystallinity. However, no obvious Pd diffraction peaks are observed for PdSn-TaN/C and Pd-TaN/C, which can be explained by the such intense diffraction peaks of nitrides and/or the low contents of Pd, similar to previous reports [32]. For the PdSn/C and commercial Pd/C catalysts, they exhibit a similar broad diffraction peak near 25° and a small peak near 40°, which are assigned to amorphous carbon and 111 reflection of Pd, respectively. In order to further investigate the composition, Raman

spectroscopy is measured and shown in Fig. 2(a,b). Similarly, as can be seen from Fig. 2(b), all the catalysts exhibit two typical carbon peaks at 1334 cm<sup>-1</sup> and 1594 cm<sup>-1</sup> assigned to D band and G band, which further confirms that carbon is present in all the catalysts [41]. For PdSn-TaN/C and Pd-TaN/C, typical tantalum nitride peaks can also be observed at the Raman shift below 800 cm<sup>-1</sup> (181, 230, 594 and 640) besides the carbon peaks (Fig. 2(a)) [31,42], consistent with the the XRD analysis of TaN crystalline phase.

To probe the nanostructure and morphology of the catalysts, TEM and HRTEM characterizations are further conducted. Fig. 3(a-c) presents the well-dispersed TEM images of the PdSn-TaN/C, Pd-TaN/C and PdSn/C catalysts without obvious agglomeration. It can be found that PdSn-TaN/C and Pd-TaN/C exhibit the similar nonaparticle size of 2.4 nm or so, while PdSn/C shows a slightly increased value of around 2.6 nm, which demonstrates that TaN can help to slightly reduce the size to some extent. The HRTEM and EDS analysis of PdSn-TaN/C are shown in Fig. 3(d-t). Specifically, HRTEM images in Fig. 3(d-k) present the clear lattice distances of around 0.195 nm, 0.229 nm and 0.15 nm ascribed to the Pd(200), Pd(111) and TaN(300) reflections, respectively, which is consistent with the good crystallinity confirmed by XRD results. The corresponding FFT (fast Fourier transform) patterns in Fig. 3(g) also suggest the exposed Pd(200) and Pd(111). Additionally, Fig. 3(e) indicates that there are abundant steps sites on the surface, similar to the reported results [43–46]. These low-coordinated Pd can be ascribed to the interactions of sodium citrate in alkaline ethylene glycol solution with abundant oxygen-containing functional groups [47]. In the meanwhile, obvious lattice mismatches are also found in Fig. 3(i), which can easily bring the variance in electronic structures of the bimetallic catalysts [48–50]. The EDS mapping images in Fig. 3(l-o) indicate that Pd (red) and Sn (blue) are uniformly distributed over the surface. It can also be found that most of Ta (magenta) is predominantly located in the outer region of C (yellow), forming a core-shell like structure, similar to our previous reports on PdCu-TaN/C [32]. Taking into account their structural advantages of the large BET area and mesoporous properties (TaN/C shows a mesoporous structure (pore of 9.7 nm) with a BET area of 81.9 m<sup>2</sup> g<sup>-1</sup>), the unique structure can be beneficial for offering a good metal/nitrides interface, as indicated by previous reports [29,32,51]. For further probing the surface structure and reaction sites of PdSn-TaN/C, DRIFTS is carried out and the result is shown in Fig. S2. Three bands at around 2170, 2117 and 2059 cm<sup>-1</sup> can be observed. The former two bands at 2170 and 2117 cm<sup>-1</sup> are associated with the gaseous CO [52], and the band at 2060 cm<sup>-1</sup> is attributed to the linearly adsorbed CO on low-coordinated Pd, consistent with HRTEM results [52–57].

To provide more interface information, XPS measurement is applied to explore the properties and variance in electronic structure. The carbon spectrum is used to correct the charge of all the samples. The Pd 3d spectrum in Fig. 4(a, b) is deconvoluted into two regions at around 336.2 and 341.52 eV, which are attributed to Pd 3d<sub>5/2</sub> and Pd 3d<sub>3/2</sub>, respectively. Each of Pd 3d<sub>5/2</sub> and Pd 3d<sub>3/2</sub> can be fitted by Pd<sup>δ+</sup> and element Pd. According to the element Pd of Pd-TaN/C at 336.31 eV and PdSn/C 336.19 eV, the variances of binding energy suggest that there exists an electronic interaction between them, in which the addition of Sn will transfer electrons to Pd, and TaN vice versa (Table S2). Besides, as depicted by Fig. 4(a, b), for all the catalysts, element Pd accounts for a predominant part. It can also be found that the addition of Sn brings a slight increase of the high-valence Pd by comparing PdSn-TaN/C and Pd-TaN/C, which can be ascribed to the fact that the oxophilic property of Sn is higher than that of Pd [58]. Similarly, the Sn 3d spectra in Fig. 4 (c) are also split into high-valence Sn at 487.41 eV and element Sn at 485.69 eV. It can be found that Sn<sup>δ+</sup> contributes almost 90.6% of Sn region, thus Sn<sup>δ+</sup> is predominantly present in the PdSn-TaN/C catalyst. Concerning the Ta 4f region in Fig. 4(d), they can be split into three peaks assigned to N-Ta-N (the valence state of Ta < +5) at 24.56 eV, N-Ta-O at 26.32 eV and O-Ta-O (the valence state of Ta is +5) at 27.15 eV [29,31,51,59]. Compared with Pd-TaN/C, PdSn-TaN/C shows

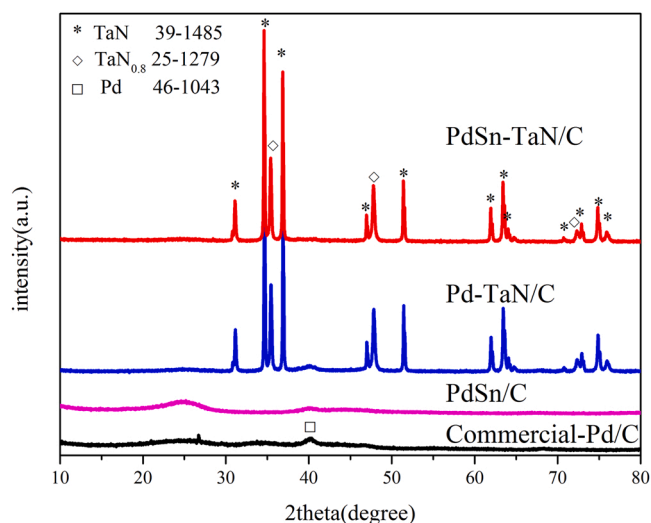


Fig. 1. XRD patterns of the PdSn-TaN/C, Pd-TaN/C, PdSn/C and commercial Pd/C catalysts.

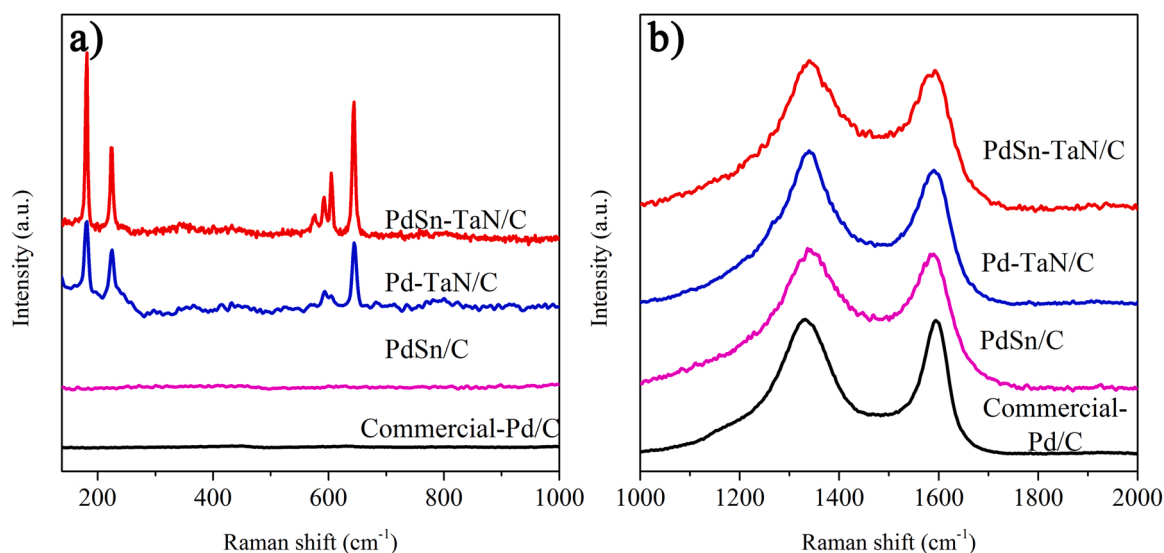


Fig. 2. Raman spectra of the PdSn-TaN/C, Pd-TaN/C, PdSn/C and commercial Pd/C catalysts.

an increase in the percentage of O-Ta-O bonds at 28.17 eV and a reduce in the percentage of N-Ta-O bonds at 26.32 eV. The differences suggest that the presence of oxophilic element of Sn brings a strengthened interaction between PdSn and TaN. Moreover, compared with Pd-TaN/C, it is observed that the binding energy of N-Ta-O and O-Ta-O in PdSn-TaN/C decrease after the presence of Sn, which may be attributed to that the resulting generation of Ta-O-Pd(Sn) weakens the Ta-O bond, thereby decreasing the binding energy. Similar interactions (i.g. Ta-O-Co, Ti-O-Co) are also published previously [29]. With respect to the O 1s spectra in Fig. 4(e), they are deconvoluted into -O- species (lattice oxygen) at around 530.7 eV, -OH species at 532.61 eV and adsorbed H<sub>2</sub>O species at 534.15 eV [60–66]. By comparing these catalysts, it can be found that the addition of TaN brings a significant increase of -O- species (23.00% of the PdSn-TaN/C, 22.21% of the Pd-TaN/C, 4.47% of the PdSn/C), while the addition of Sn brings a obvious increase of -OH species (63.39% of the PdSn-TaN/C, 59.94% of the Pd-TaN/C, 81.33% of the PdSn/C). Thus it can be suggested that the TaNO/TaO contributes predominantly to the -O- species, and the oxophilic Sn tends to increase the -OH species on the surface. In conclusion, the XPS measurements indicate that a modulated electronic interaction has been formed between PdSn and TaN, further confirming the interfacial interaction between PdSn and TaN.

Overall, combining Drifts and HRTEM characterization, it is demonstrated that PdSn-TaN/C with a core-shell like structure is composed of the low-coordinated Pd sites on the surface due to the lattice mismatches and interface effects. XPS characterization further confirm the existed electronic interaction between them. Benefited from the unique structure, PdSn-TaN/C is expected to become a promising catalyst for high-efficient EOR in the alkaline media by the interfacial interaction between PdSn and TaN.

### 3.2. Electrocatalytic ethanol oxidation on the PdSn-TaN/C, Pd-TaN/C, PdSn/C and commercial Pd/C catalysts

Based on the above structural characteristics, it can be predicted that the PdSn-TaN/C will exhibit good catalytic performances. Before the EOR measurements, the CV curves of the PdSn-TaN/C, Pd-TaN/C, PdSn/C and commercial Pd/C catalysts are performed in a nitrogen-saturated electrolyte with 1 M KOH, as shown in Fig. 5(a) and Fig. S3. Generally speaking, the peaks in the potential regions of 0–0.35 V, 0.35–0.55 V and 0.55–1.2 V are assigned to the adsorption/desorption peaks of hydrogen, the double-layer capacitance and the formation/reduction peaks of Pd oxides (OH adsorption, Pd-O), respectively [9,12,41,67–71].

For the formation of Pd-OH at around 0.6 V, the order of onset-potential position of these catalysts is PdSn-TaN/C (0.56 V) < PdSn/C (0.59 V) < Pd-TaN/C (0.62 V) < Pd/C (0.78 V). The lowest onset potential of Pd-OH<sub>ad</sub> for PdSn-TaN/C among these catalysts indicates that OH is easily formed on the surface, which can be attributed to the oxophilic property of Sn [28,72]. Compared with Pd/C, the decrease of the onset potential of Pd-OH<sub>ad</sub> for Pd-TaN/C demonstrates that the doped TaN also facilitates the generation of OH to some extent, which can further help to remove the poisoned species and release the Pd active sites [3].

Then, the alkaline EOR performance of these catalysts are investigated in a 1 M ethanol + 1 M KOH solution with Ar bubbled, in which the Pd-TaN/C, PdSn/C and commercial Pd/C catalysts are chosen to clarify the effects of TaN and Sn. Fig. 5(b) shows the mass activities towards alkaline EOR based on the of Pd loading. Remarkably, PdSn-TaN/C presents an extremely high mass activity of 13,025.84 mA mg<sub>Pd</sub><sup>-1</sup>, which is considerably higher than those of Pd-TaN/C (10,829.96 mA mg<sub>Pd</sub><sup>-1</sup>), PdSn/C (4922.71 mA mg<sub>Pd</sub><sup>-1</sup>), Pd/C (484.21 mA mg<sub>Pd</sub><sup>-1</sup>) catalysts, and is also superior to most EOR electrocatalysts containing Pd published so far (listed in Table S3) [1]. The good mass activity can be explained by the larger ECSA of PdSn-TaN/C (200.37 m<sup>2</sup> g<sup>-1</sup>) than Pd-TaN/C (167.77 m<sup>2</sup> g<sup>-1</sup>), PdSn/C (97.34 m<sup>2</sup> g<sup>-1</sup>) and Pd/C (42.23 m<sup>2</sup> g<sup>-1</sup>) catalysts, which is estimated from the area of the integrated CO oxidation peak in the CO stripping tests (Supporting information). The detailed activity values are summarized in Table 1. This result also highlights that the addition of TaN can dramatically increase the exposure of active sites. At the same time, considering that the mass activity of Pd-TaN/C also exceeds the PdSn/C (almost 2.2 times) and Pd/C (almost 22.4 times) catalysts, it can be concluded that TaN plays a critical role in accelerating the alkaline EOR activity, which may be due to the unique interfacial interaction with core-shell like structure, as verified by HRTEM and XPS results. Moreover, the ECSA-based specific activity is 6.50 mA cm<sub>Pd</sub><sup>-2</sup> for PdSn-TaN/C, higher than those of Pd-TaN/C (6.46 mA cm<sub>Pd</sub><sup>-2</sup>), PdSn/C (5.06 mA cm<sub>Pd</sub><sup>-2</sup>) and commercial Pd/C (1.15 mA cm<sub>Pd</sub><sup>-2</sup>) catalysts, which demonstrates its enhanced intrinsic activity. In a word, compared with the Pd-TaN/C, PdSn/C and Pd/C catalysts, the outstanding catalytic performance of PdSn-TaN/C catalyst towards alkaline EOR can be correlated with its prominent structural advantages, that is, the construction of PdSn-TaN/C interface brings a tunable electronic structure, verified by HRTEM, EDS, XPS and DRIFTS results.

Regarding the reaction kinetics, the onset potential of PdSn-TaN/C acquired from linear sweep voltammogram (LSV) shown in Fig. 5(c) is 0.34 V, lower than other catalysts, demonstrating that ethanol is rapidly



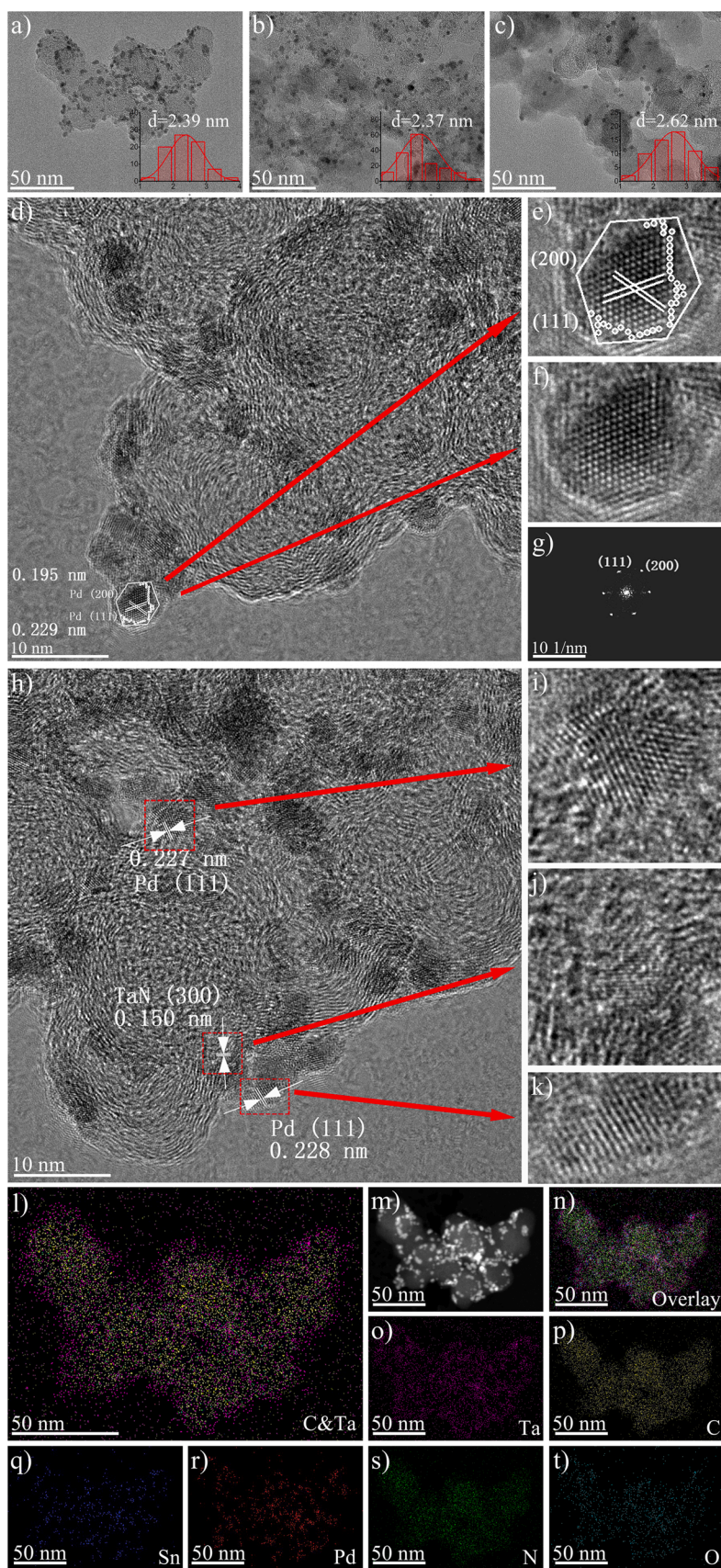


**Fig. 3.** (a-c) TEM images of the synthesized PdSn-TaN/C, Pd-TaN/C and PdSn/C catalysts. (d-k) HR-TEM images of the Pd<sub>1</sub>Sn<sub>3</sub>-TaN/C-m-alkaline catalyst ((e, f, i-k) the magnified images of the white or red rectangular frame, (g) the FFT pattern of the white rectangular frame in Fig. 3(d)). (l-t) the corresponding EDS element mapping images of the PdSn-TaN/C catalyst.

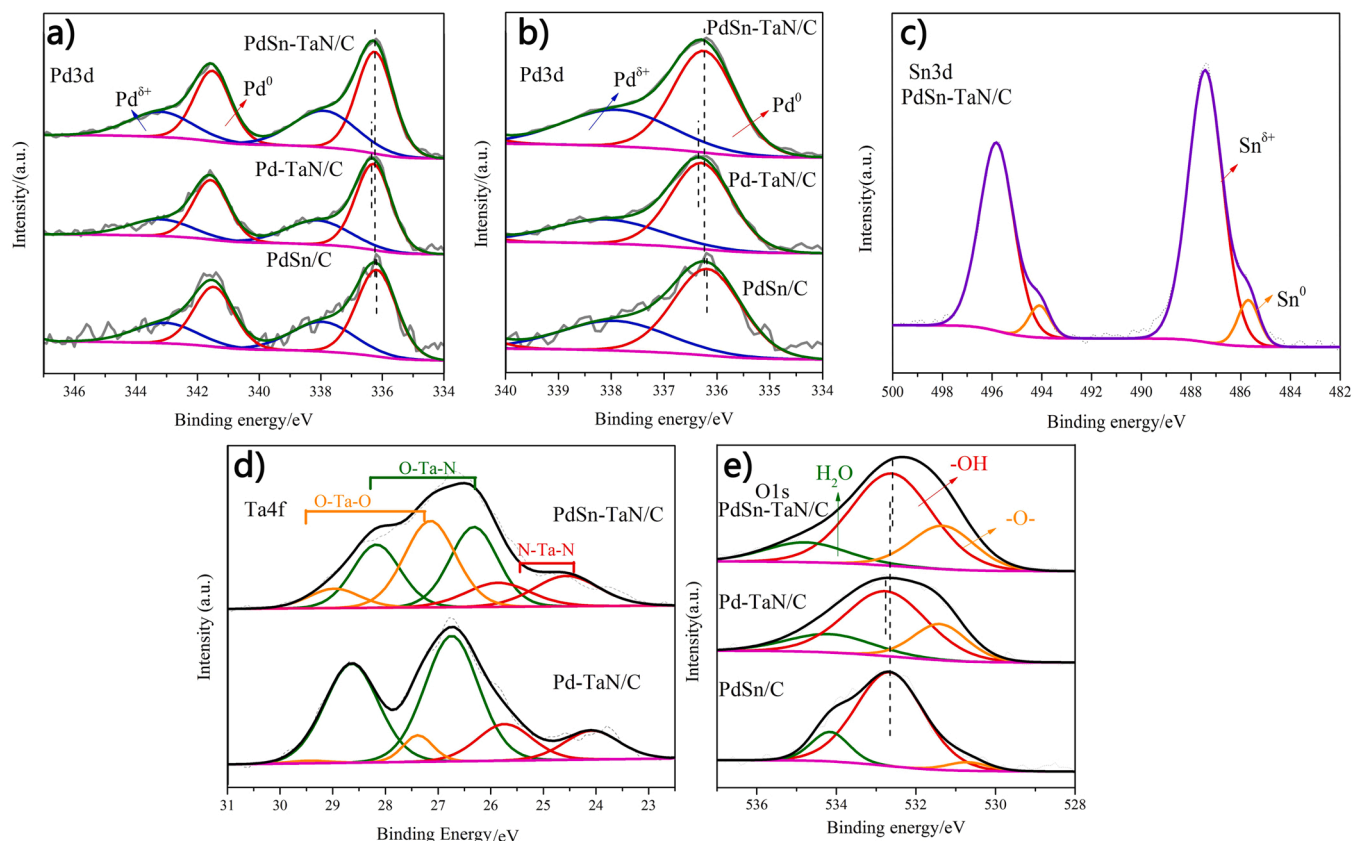


**Fig. 4.** High-resolution XPS spectra of the (a) Pd3d (b) the enlarged images of Fig. 4(a), (c) Sn3d, (d) Ta4f and (e) O1s region of the synthesized PdSn-TaN/C, Pd-TaN/C and PdSn/C catalysts.

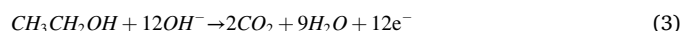
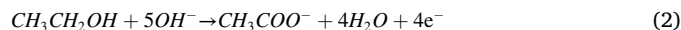
oxidized on the surface of PdSn-TaN/C in alkaline medium. As for the charge transfer kinetics, Electrochemical impedance spectroscopy (EIS) measurements are also performed and Fig. 5(d) and Fig. S4. shows the corresponding Nyquist plots with simplified Randles equivalent circuits and bode plots towards alkaline EOR. The  $R_{ct}$  of PdSn-TaN/C is smaller than any other catalysts, which indicates good charge transfer ability [73].

For the durability of these catalysts, Fig. 5(e) shows the Chronoamperometric (CA) plots of alkaline EOR at 0.74 V for 3600 s. PdSn-TaN/C always presents higher activity and slower activity decay than other catalysts throughout the process, and the durability of PdSn-TaN/C is also superior to most EOR electrocatalysts containing Pd published so far (listed in Table S4), which can be ascribed to its good resistance to CO-like poisoning intermediates. One of the reasons for the improved kinetics and durability of PdSn-TaN/C is the facile formation of OH species on its surface by the dissociation of water (i.g. benefited from the oxophilic property of Sn), which agrees well with the CV and in situ ATR-SEIRAS results [74].

### 3.3. In situ observation of intermediates of EOR in alkaline media

To elucidate the possible reaction pathways and uncover the reaction mechanism by means of the identification of intermediates and/or products for alkaline EOR, In situ ATR-SEIRAS is performed. The assignments of In situ ATR-SEIRAS bands are summarized in Table 2 in detail. On the base of the reported results, the band located at around 1050  $\text{cm}^{-1}$  represents the C—OH stretching vibration mode of ethanol (shown in Fig. S5) [2,14,15,26,46,50,69,70,75–77]. Fig. 6 shows In situ ATR-SEIRAS spectra at 2250–1290  $\text{cm}^{-1}$  and the corresponding fitted bands at around 1400  $\text{cm}^{-1}$  of these catalysts during EOR with the reference spectra at 0 V [75]. Specifically, the bands at 1416 and 1550  $\text{cm}^{-1}$  in Fig. 6(a, c, e, g) are assigned to the symmetric and

asymmetric stretching of O—C—O, a feature of acetate ions ( $\text{CH}_3\text{COO}^-$ ), which are generated from the incomplete oxidation process as C2 pathway products (a 4-electron conversion), as shown in the following Eq. 2, respectively [2,4,14,17,20,27,50,69,70,78–85]. The band at 1394  $\text{cm}^{-1}$  belongs to carbonate ( $\text{CO}_3^{2-}$ ), which is an indicator of the completely oxidized products of C1 pathway for alkaline EOR (a 12-electron conversion), as shown in Eq. 3 below [4,8,11,13,17,25,27,69,79,82,84,86].



These identification of the bands suggests that, for these catalysts in this work, the electro-oxidation of alkaline ethanol occurs through two pathways: a total oxidation to carbonate and a partial oxidation to acetate, coincided with the literature [77,84]. In view of the overlaps of the bands at 1416 and 1394  $\text{cm}^{-1}$ , they are deconvoluted into two Gaussians bands shown in Fig. 6(b, d, f, h) as a function of the potential [11]. In addition, the weak and broad band at 1346  $\text{cm}^{-1}$  can be assigned to the bending vibration of C—H in  $\text{HCOO}^-$ , which is different from the narrow band close to 1346  $\text{cm}^{-1}$  of  $\text{CH}_3\text{COO}^-$  species, consistent with the previous results [11]. The band positioned close to 1620  $\text{cm}^{-1}$  is related to the bending deformations of interfacial  $\text{H}_2\text{O}$ , whose intensity is so intense that the bands at 1600–1800  $\text{cm}^{-1}$  are affected [26,71,78,87,88]. Therefore, the bands corresponding to C=O of acetaldehyde and acetyl at around 1620  $\text{cm}^{-1}$  are overlapped and difficult to be distinguished [26,80,83,87–89]. The two bands located between 2010 and 2110  $\text{cm}^{-1}$  are attributed to linearly bonded CO, which can be ascribed to  $\text{CO}_{ads}$  on different active sites [28,46,75,90–94]. As reported previously, the adsorbed CO is the consequence of



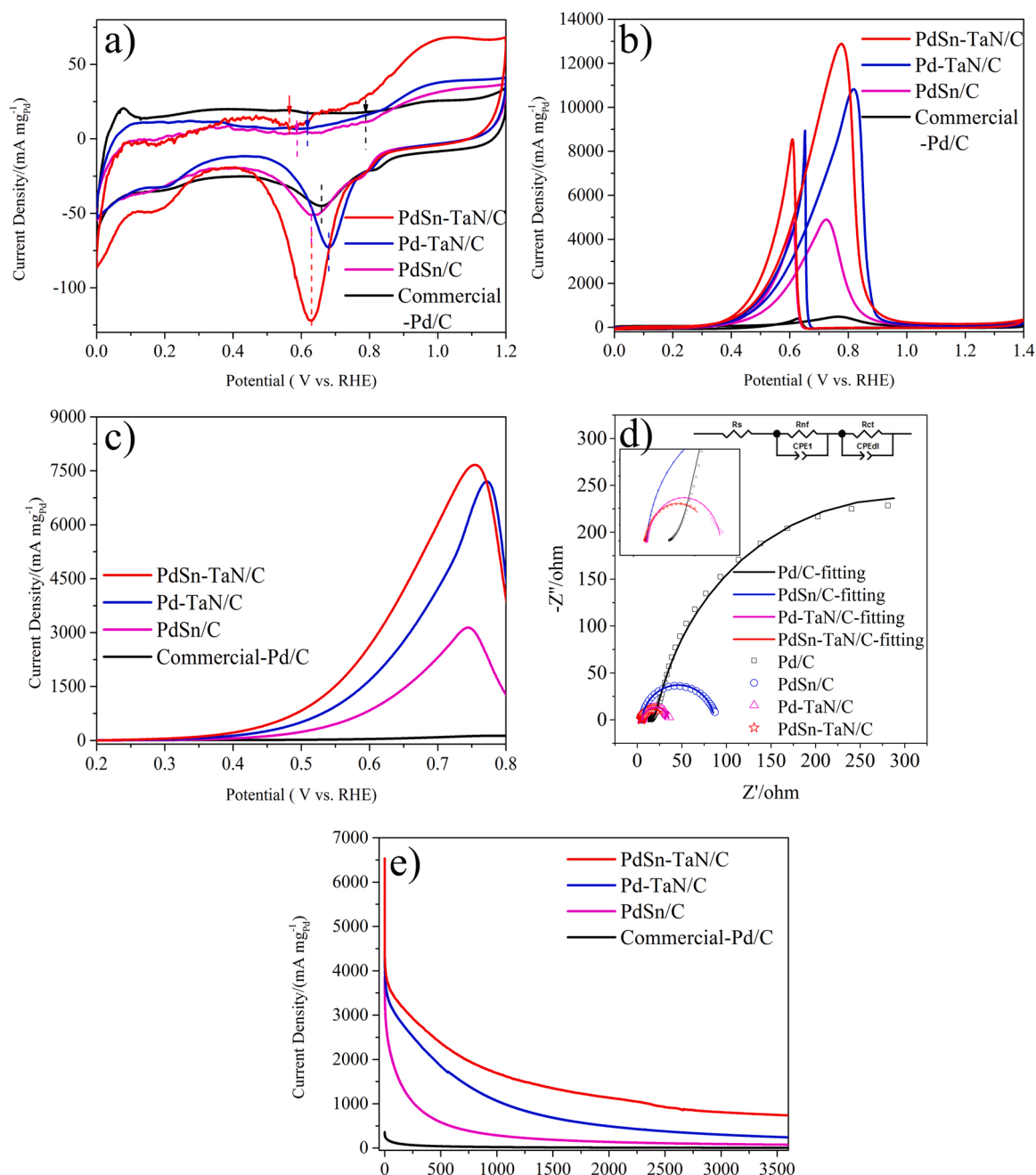


**Fig. 5.** (a) CV curves in a 1 M KOH of the PdSn-TaN/C, Pd-TaN/C, PdSn/C and commercial Pd/C catalysts at 50 mV/s. (The arrows in Fig. 5a in the positive scan represent the onset potential of Pd-OH<sub>ad</sub>, and the dash lines in the negative scan represent the peak potential of PdO reduction peak.) (b) CV curves in a 1 M KOH/1 M ethanol solution of the PdSn-TaN/C, Pd-TaN/C, PdSn/C and commercial Pd/C catalysts at 50 mV/s. (c) LSV curves at 10 mV/s, (d) Nyquist plots at 0.66 V and (e) CA tests at 0.74 V of the PdSn-TaN/C, Pd-TaN/C, PdSn/C and commercial Pd/C catalysts in an Ar-purged 1 M KOH/1 M ethanol solution.

**Table 1**

Comparison of the performances with the PdSn-TaN/C, Pd-TaN/C, PdSn/C and commercial Pd/C catalysts for EOR in alkaline media.

Materials	ECSA (m <sup>2</sup> g <sup>-1</sup> )	EOR	
		I <sub>p</sub> (m)/ (mA mg <sub>Pd</sub> <sup>-1</sup> )	I <sub>p</sub> (sa)/ (mA cm <sub>Pd</sub> <sup>-2</sup> )
PdSn-TaN/C	200.37	13,025.84	6.50
Pd-TaN/C	167.77	10,829.96	6.46
PdSn/C	97.34	4,922.71	5.06
Commercial Pd/C	42.23	484.21	1.15

the dissociative chemisorptions of ethanol [11,69,89,95]. Given that CO will be completely oxidized at high potential, the spectra are also displayed in Fig. S6(a, c, e, g) with the reference spectra at 1.4 V to observe the variance of CO dependent on the potential. We can find that the adsorbed CO gradually fades with the increased applied potential due to the oxidative removal for all the catalysts [80]. Additionally, It can also be found that the position of the CO band increases as a function of the growing potential, which can be ascribed to the Stark effects, the metal-induced back donation or the lateral interactions [75,79,96]. Furthermore, the corresponding spectra at 4000–3000 cm<sup>-1</sup> are shown in Fig. S6(b, d, f, h), which represents the vibration of interfacial water. And the broad band at 2500–3000 cm<sup>-1</sup> is assigned to the C–H

**Table 2**

Assignments of In situ ATR-SEIRAS bands observed in spectra for alkaline EOR.

Wavenumbers/cm <sup>-1</sup>	assignments
~1050	$\nu(\text{C}-\text{OH})$ of surface $\text{CH}_3\text{CH}_2\text{OH}$
~1346	$\delta(\text{C}-\text{H})$ in acetate ions $\text{HCOO}^-$
~1394	carbonate ( $\text{CO}_3^{2-}$ )
~1416	$\nu(\text{O}-\text{C}-\text{O})$ of symmetric acetate ions ( $\text{CH}_3\text{COO}^-$ )
~1550	$\nu(\text{O}-\text{C}-\text{O})$ of asymmetric acetate ions ( $\text{CH}_3\text{COO}^-$ )
~1620	$\delta(\text{H}-\text{O}-\text{H})$ of interfacial $\text{H}_2\text{O}$
~1700	$\nu(\text{C}=\text{O})$ of acetaldehyde and acetyl
2010–2110	$\nu(\text{C}-\text{O})$ of $\text{CO}_{\text{ad}}$ (linear-bonded CO band)
2500–3000	$\nu(\text{C}-\text{H})$ stretching of adsorbed $\text{CH}_3\text{CH}_2\text{OH}$
3000–3700	$\nu(\text{O}-\text{H})$ of $\text{H}_2\text{O}$ and interfacial water

 $\nu$ : stretching vibration;  $\delta$ : bending vibration.

stretching vibrations in ethanol and/or intermediates [4,13,71,76,77,79,81,89].

To evaluate the energy efficiency of the corresponding catalysts, the method proposed by Liang et al. is employed to determine the  $\text{CO}_2$  selectivity according to the following equation of  $C_{\text{carbonate}}/(C_{\text{carbonate}} + C_{\text{acetate}}) = 6A_{1394} / (6A_{1394} + 4A_{1400} \times 2.2)$ , where 6 and 4 represent the numbers of electron transfer for one  $\text{CO}_3^{2-}$  and one  $\text{CH}_3\text{COO}^-$ , 2.2 represents the ratio of absorbance coefficient per mole of  $\text{CO}_3^{2-}$  and  $\text{CH}_3\text{COO}^-$  [11]. The corresponding  $\text{CO}_3^{2-}$  selectivities of these catalysts as a function of the potential, which reflects high ethanol utilization efficiency related to the complete EOR, are displayed in Fig. 7(a). Here, the presented  $\text{CO}_3^{2-}$  selectivity are compromised parameters for assessing the proportion of the total oxidation [83,97]. It is found that the selectivity of carbonate for PdSn-TaN/C (around 20.5%) in all potentials is higher than those of Pd-TaN/C (around 14.1%), PdSn/C (around 8.7%) and Pd/C (0%), indicating that the cleavage of C-C bond is favourable on the PdSn-TaN/C surface, which is in agreement with its superior catalytic current density (Fig. 7(b)). The low  $\text{CO}_3^{2-}$  selectivities of Pd/C can be due to high CO contents and sluggish CO oxidation kinetics, in accord with the previous reports [16]. In addition, Pd-TaN/C gives a higher  $\text{CO}_3^{2-}$  selectivity compared to PdSn/C. These results indicate that the presence of TaN can efficiently enhance the C-C bond cleavage relative to the presence of Sn, supporting the previous CV results. It can also be found that the  $\text{CO}_3^{2-}$  selectivities show a slightly falling trend as the potential increases, which may be attributed to the lack of the Pd active sites induced by the surface oxidation at high potentials [75,88,98].

To further understand the possible reaction pathways and the effects of TaN and Sn, the relationship between the intensity of CO as an important intermediate and the applied potential is also investigated shown in Fig. 7(c). It is found that the disappearance of the CO band for commercial Pd/C is at around 1.32 V, which is much higher than those for PdSn-TaN/C (0.85 V), Pd-TaN/C (0.94 V) and PdSn/C (0.85 V). The intensity of the integrated CO absorbance is highest for the commercial Pd/C. A large amount of CO will obstruct the release of Pd active sites and the subsequent oxidation, leading to low selectivity of  $\text{CO}_3^{2-}$  [75]. Compared with Pd/C, the additions of TaN and Sn will shorten the CO potential region and decrease the intensity of CO bands, proving that the anti-CO poisoning ability is enhanced [95]. The limited potential range of CO band also implies that the surface will be relieved at a larger potential range owing to the absence of strongly adsorbed CO. This may be due to the facilitated formation of OH, confirmed by the previous CV results and the later OH bands in the in-situ ATR-SEIRAS results, which can react with CO and reduce the poisoning effect as the bi-functional theory said [13,75,99,100].

From both quantitative and qualitative perspectives, the dependence of both the integrated OH intensity and the percentage of integrated OH intensity at  $3600\text{ cm}^{-1}$  in interfacial water ( $3800\text{--}3200\text{ cm}^{-1}$ ) on the potential can be seen in Fig. 7(d) and (e), respectively. Here, the OH intensity at  $3600\text{ cm}^{-1}$  is one of three deconvoluted gaussian bands of the interfacial water. The relationships between the detailed fitted bands and the applied potentials are as shown in Fig. S7-S9 and Table S5-S8. As

shown in Fig. 7(d), the integrated OH intensities remain almost stable from 0 to 0.6 V, and then rapidly drop after 0.6 V. Then, as a representative, Fig. 7(f) shows the fitted bands at  $4000\text{--}3000\text{ cm}^{-1}$  of these catalysts at 0.47 V (stable period) to clarify the corresponding trends of the three bands. Specifically, according to previous reports, the deconvoluted bands at  $3600$ ,  $3450$  and  $3270\text{ cm}^{-1}$  are assigned to the dangling O-H bond (non-hydrogen-bonded adsorbed water), trihedrally-coordinated water (weakly hydrogen-bonded water molecules) and tetrahedrally-coordinated water (strongly hydrogen-bonded ice-like water molecules), respectively [91,96,101–108]. It is generally believed that the dangling O-H bond can oxidize CO according to the bi-functional theory (i.g. Langmuir-Hinshelwood (H-L) mechanism, Eley-Rideal mechanism (E-L) mechanism), thus leading to the enhanced tolerance to CO and the regeneration of Pd active sites [9,13,50,67,84,99,100]. This can be supported by the fact that, as shown in Fig. 7(c, d), the integrated CO intensity declines as the potential increases, which is accompanied by the descent of the OH intensity with the increasing potential, matching well with the previous results [91,105,109]. As shown in Fig. 7(d, e), it is also found that from both quantitative and qualitative perspectives, both the integrated OH intensity and the percentage of integrated OH intensity at  $3600\text{ cm}^{-1}$  for PdSn-TaN/C are higher than that of Pd-TaN/C and PdSn/C, which proves that PdSn-TaN/C is more active in the formation of OH, consistent with the lower onset potential of the OH formation in CV measurements. This is also responsible for the fast CO oxidation kinetics and the resulting remarkable catalytic performance of PdSn-TaN/C, as revealed by in situ ATR-SEIRAS and CV results. However, for commercial Pd/C, the deconvoluted band at  $3600\text{ cm}^{-1}$  corresponding to OH is almost negligible, and only the band at  $3450\text{ cm}^{-1}$  corresponding to trihedrally coordinated water can be observed. The above results can explain the large CO potential region and sluggish CO removal kinetics of commercial Pd/C. Note that the percentages of integrated OH intensity at  $3600\text{ cm}^{-1}$  in Fig. 7(e) firstly stay unchanged, followed by an upward trend during the later period. This is attributed to that the positions of the interfacial water bands show a positive shift as the applied potential increases, consistent with the trends in Fig. S6(b, d, f, h).

By combining with the above in situ ATR-SEIRAS and CV results, it is found that the promoting effects of TaN and Sn are obvious but different. One can see that, by comparing PdSn/C and Pd-TaN/C, Pd-TaN/C shows an enhanced selectivity toward  $\text{CO}_3^{2-}$  formation and high activity. However, one can also found that Pd-TaN/C shows a higher CO disappearance potential and a lower OH intensity and OH intensity percentage than PdSn/C. The results indicate that the modification of TaN can effectively cleave the C-C bonds and thus improve the activity although it does not significantly enhance the OH formation like Sn. On the contrary, the modification of Sn can enhance the tolerance to CO by the larger amounts of OH formation (also as verified by the CO stripping results later), but can not substantially improve the  $\text{CO}_3^{2-}$  selectivity and activity like TaN. Obviously, compared with Pd-TaN/C, the high anti-poisoning ability induced by the enhanced OH band of PdSn/C contradicts its lower activity shown in CV results. The difference may depend on their capability to cleave the C-C bonds. Specifically, for Pd/C, no carbonate band is observed, only acetate and CO bands are observed by in situ ATR-SEIRAS measurements, demonstrating that Pd/C shows a preference for the partial oxidation of ethanol, which is responsible for the poor catalytic performance. The slow CO oxidation kinetics along with the lower OH on the Pd/C surface also account for the poor catalytic performance of Pd/C. Compared with Pd/C, PdSn/C shows an improved  $\text{CO}_3^{2-}$  selectivity. In view of the large amounts of CO on the Pd/C surface from the dissociative chemisorptions of ethanol, the improved  $\text{CO}_3^{2-}$  selectivity of PdSn/C can be explained by that the Sn modification can accelerate the further oxidation of pre-adsorbed CO by the OH species. Remarkably, the process is almost not related to the further C-C bond splitting, which supports the above contradiction between the high amounts of OH and high selectivity to  $\text{CO}_3^{2-}$  of PdSn/C. Compared with Pd/C and PdSn/C, the higher  $\text{CO}_3^{2-}$  selectivity of Pd-TaN/C



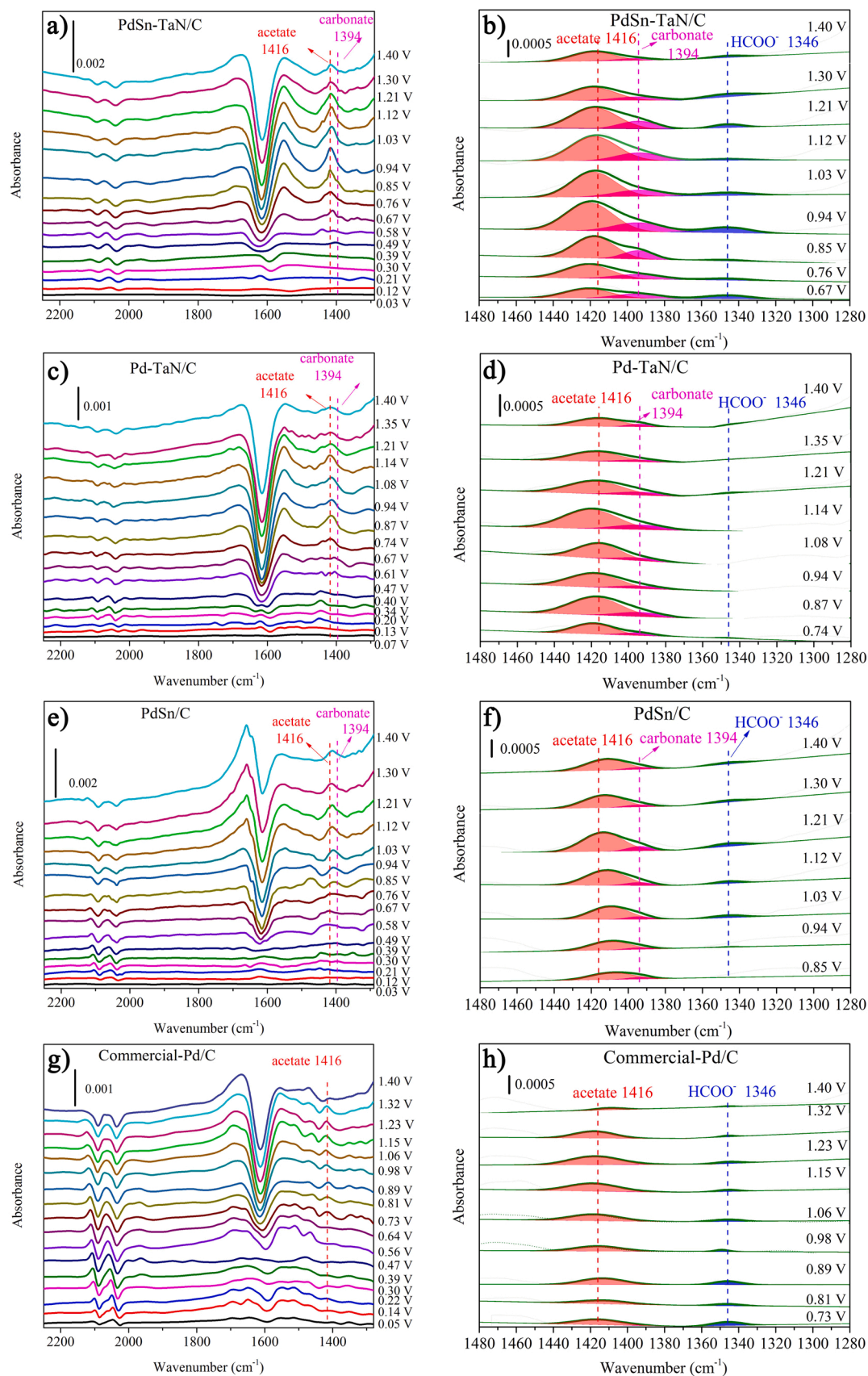


**Fig. 6.** In situ ATR-SEIRAS spectra of the PdSn-TaN/C (a), Pd-TaN/C (c), PdSn/C (e) and commercial Pd/C catalysts (g) during EOR (the reference spectra are at 0 V). The fitted bands at 1480–1280  $\text{cm}^{-1}$  of the PdSn-TaN/C (b), Pd-TaN/C (d), PdSn/C (f) and commercial Pd/C (h) catalysts.

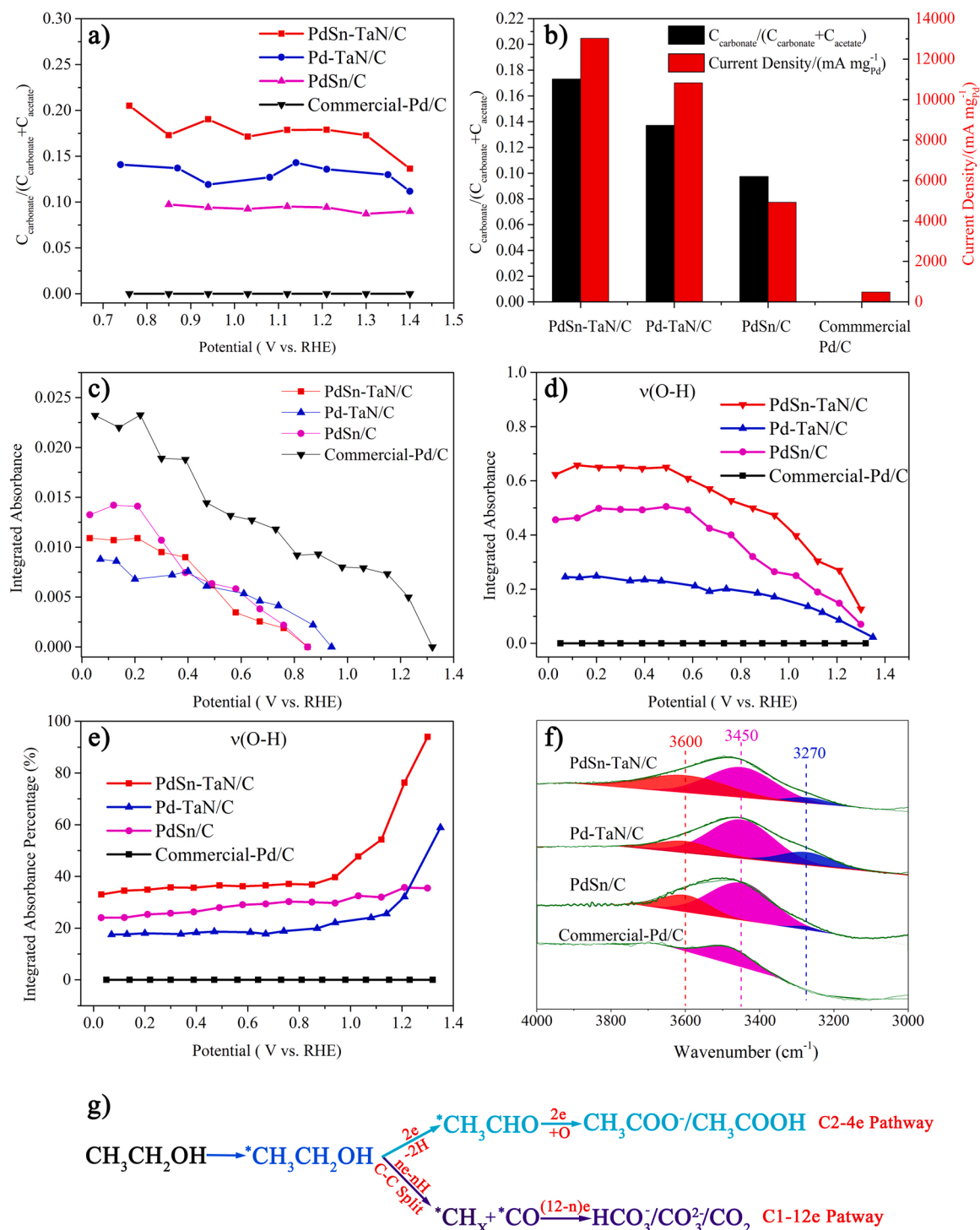


**Fig. 7.** (a) the potential dependence of the selectivity of carbonate; (b) the potential dependence of the selectivity of carbonate (left axis) and catalytic activity (right axis) for PdSn-TaN/C, Pd-TaN/C, PdSn/C and commercial Pd/C catalysts; (c) plots of potential-dependent intensities of the integrated CO absorbance; (d) dependence of the integrated absorbance of OH on the potential; (e) the integrated absorbance percentage of the OH as a function of the potential; (f) The fitted bands at 4000–3000 cm<sup>-1</sup> of these catalysts and (g) reaction pathways of intermediates for ethanol oxidation in alkaline medium.

C suggests that TaN can further break the C—C bonds except the initial dissociative chemisorptions of ethanol. Consequently, we can also conclude that OH mainly plays a role in enhancing the CO oxidation kinetics, and then promotes the improvement of catalytic performance. However, OH may be not the only descriptor for the high activity, whose finite improvement is limited by the C-C cleavage of ethanol molecules. That is, hydroxyl is a sufficient and unnecessary condition for increasing the CO<sub>3</sub><sup>2-</sup> selectivity. Therefore, the positive effect of TaN on the C-C

splitting is also highlighted.

Overall, in situ ATR-SEIRAS experiments display that alkaline EOR occurs on these catalysts by complete oxidation to CO<sub>3</sub><sup>2-</sup> (a 12-electron transfer) and incomplete oxidation path to acetate (a 4-electron transfer). For the commercial Pd/C, the only acetate band is observed, demonstrating that EOR predominantly occurs on Pd/C via incomplete ethanol electro-oxidation to acetate. After the addition of TaN and Sn, PdSn-TaN/C exhibits both the best catalytic activity and the highest

total oxidation efficiency among these catalysts, which may be due to the excellence of the PdSn-TaN/C interface. Note that the complete oxidation of alkaline ethanol to  $\text{CO}_3^{2-}$  contains the C—C bond splitting initially, followed by the further oxidation of the ethanol fragments into  $\text{CO}_3^{2-}$ . Specifically, the addition of TaN is of great importance to facilitate the cleavage of C—C bonds, as verified by the in situ ATR-SEIRAS. What's more, the presence of Sn can enhance the further oxidation of CO-like intermediates by the facilitated formation of the dangling O—H. According to the above analysis, we can speculate the proposed reaction pathway on PdSn-TaN/C for alkaline EOR, as shown in Fig. 7(g). In short, for PdSn-TaN/C, as the best sample among these catalysts, TaN modification helps to undergo preferentially the complete oxidation through the C—C cleavage, while Sn modification promotes the subsequent oxidation of the ethanol fragments.

### 3.4. DFT calculations

To confirm the higher selectivity of  $\text{CO}_2$  and CO tolerance of PdSn-TaN/C for EOR, based on the previous reports [14,15,24,25], DFT calculations are further conducted to investigate the adsorption configurations and adsorption energies of the key intermediates, such as  $\text{CH}_3\text{CH}_2\text{OH}$ ,  $\text{CH}_3\text{CHOH}$ ,  $\text{CH}_3\text{CHO}$ ,  $\text{CH}_3\text{CO}$ ,  $\text{CH}_2\text{CO}$ ,  $\text{CHCO}$ ,  $\text{CH}_3$ , CO and OH from ethanol dehydrogenation on the Pd(111),  $\text{Pd}_4/\text{TaN}(001)$  and  $\text{Pd}_4\text{-SnO}_2/\text{TaN}(001)$  surfaces, shown in Fig. S10-S12 and Table 3. Compared to the clean Pd(111) surface, it is found that the adsorption intensities of  $\text{CH}_3\text{CH}_2\text{OH}$ ,  $\text{CH}_3\text{CHOH}$ ,  $\text{CH}_3\text{CHO}$ ,  $\text{CH}_3$ , and OH are improved on the  $\text{Pd}_4/\text{TaN}(001)$  and  $\text{Pd}_4\text{-SnO}_2/\text{TaN}(001)$  surfaces at some extent, suggesting that the presence of TaN and Sn increases the interaction between the corresponding species and catalyst surfaces. However, the adsorption of  $\text{CH}_3\text{CO}$ ,  $\text{CH}_2\text{CO}$ ,  $\text{CHCO}$  and CO is weakened evidently with the introduction of TaN and Sn, indicating that the anti-CO and anti- $\text{CH}_3\text{CO}$  ( $\text{CH}_2\text{CO}$  and  $\text{CHCO}$ ) poisoning abilities are enhanced, agreement with the in situ ATR-SEIRAS results.

According to the previous reports [110–112], it has been considered that the  $\alpha$ -C—H bonds in the adsorbed ethanol decomposition fragments are prior to cleave on the Pd-based catalysts. Therefore, to investigate the C—C bond cleavage mechanism of EOR on the prepared catalysts, the adsorbed  $\text{CH}_3\text{CH}_2\text{OH}$  at the top site is selected as the starting state and the formation of  $\text{CH}_3\text{CO}$  is considered to go through a three-step oxidation process ( $\text{CH}_3\text{CH}_2\text{OH}$ - $\text{CH}_3\text{CHOH}$ - $\text{CH}_3\text{CHO}$ - $\text{CH}_3\text{CO}$ ) during EOR, as shown in Fig. 8(a). After calculating and comparing the energy barriers of three elementary reactions on three surfaces (Table S9), it is found that the activation energies of three reactions are only 0.72, 0.65 and 0.48 eV on the  $\text{Pd}_4\text{-SnO}_2/\text{TaN}(001)$  surface, which are lower than the values on Pd(111) and  $\text{Pd}_4/\text{TaN}(001)$ . Compared with Pd(111), it is indicated that the activation energies are also lower with the values of 0.95, 0.75 and 0.56 eV. The results suggest that the presence of Sn and TaN promotes the dehydrogenation of  $\text{CH}_3\text{CH}_2\text{OH}$ ,  $\text{CH}_3\text{CHOH}$  and  $\text{CH}_3\text{CHO}$ , leading the enhancement of catalytic activity for EOR, consistent with the CV results.

**Table 3**

The adsorption energies ( $E_{\text{ads}}$ , eV) of  $\text{CH}_3\text{CH}_2\text{OH}$ ,  $\text{CH}_3\text{CHOH}$ ,  $\text{CH}_3\text{CHO}$ ,  $\text{CH}_3\text{CO}$ ,  $\text{CH}_3$ , CO and OH from the ethanol dehydrogenation on the Pd(111),  $\text{Pd}_4\text{-TaN}$  (001) and  $\text{Pd}_4\text{-SnO}_2\text{-TaN}(001)$  surfaces.

Species	Adsorption energies ( $E_{\text{ads}}$ , eV)		
	Pd (111)	Pd-TaN (001)	Pd-SnO <sub>2</sub> -TaN (001)
$\text{CH}_3\text{CH}_2\text{OH}$	-0.44	-0.58	-0.87
$\text{CH}_3\text{CHOH}$	-1.87	-2.03	-2.46
$\text{CH}_3\text{CHO}$	-0.42	-0.68	-0.94
$\text{CH}_3\text{CO}$	-2.69	-2.26	-1.85
$\text{CH}_2\text{CO}$	-1.28	-1.02	-0.67
$\text{CHCO}$	-3.34	-2.87	-2.25
CO	-2.18	-1.36	-0.85
OH	-2.26	-3.86	-4.42
$\text{CH}_3$	-1.98	-2.12	-2.54

Based on the previous DFT calculations, Li et al. [110] and Wu et al. [112] indicated that the  $\text{CH}_3\text{CO}$  and  $\text{CH}_2\text{CO}$  groups both preferred to dehydrogenate with lower C—H bond cleavage barriers on the clean Pd (111) and Pd(100) surfaces. However,  $\text{CHCO}$  favored breaking the C—C bond to generate CH and CO species. In other words, the C—C bond cleavage would start from the  $\text{CHCO}$  species for the ethanol decomposition on the Pd(111) and Pd(100) surfaces. Therefore, the C—C and C—H bonds cleavage of  $\text{CH}_3\text{CO}$ ,  $\text{CH}_2\text{CO}$ ,  $\text{CHCO}$  is studied and compared on three surfaces, as exhibited in Fig. 8 (b-d) and Table S9. The adsorbed  $\text{CH}_3\text{CO}$ ,  $\text{CH}_2\text{CO}$  and  $\text{CHCO}$  at the bridge site is selected as the initial states for all the surfaces. For  $\text{CH}_3\text{CO}_{\text{ad}}$  (Fig. 8 (b)), it can be found that the activation energies of the C—C bond cleavage are 1.48, 0.85 and 0.46 eV on the Pd(111),  $\text{Pd}_4/\text{TaN}(001)$  and  $\text{Pd}_4\text{-SnO}_2/\text{TaN}(001)$  surfaces, which are higher than the values of 0.92, 0.74 and 0.32 eV for C—H bond cleavage, indicating that the C—H bond is prior to break for  $\text{CH}_3\text{CO}$  for three surfaces. As shown in Fig. 8 (c), we can find the  $\text{CH}_2\text{CO}$  species follows the similar condition that the C—H bond is relatively easier to break. The energy barriers of the C—C bond cleavage in  $\text{CHCO}$  are corresponded to 1.17, 0.61 and 0.24 eV on the Pd(111),  $\text{Pd}_4/\text{TaN}(001)$  and  $\text{Pd}_4\text{-SnO}_2/\text{TaN}(001)$  surfaces (Fig. 8 (d)). Thus, it can be found that the energy barriers of the C—H bond cleavage in  $\text{CH}_3\text{CH}_2\text{OH}$ ,  $\text{CH}_3\text{CHOH}$ ,  $\text{CH}_3\text{CHO}$ ,  $\text{CH}_3\text{CO}$ ,  $\text{CH}_2\text{CO}$  and the C—C bond cleavage in  $\text{CH}_3\text{CO}$ ,  $\text{CH}_2\text{CO}$ ,  $\text{CHCO}$  are evidently reduced on the  $\text{Pd}_4\text{-SnO}_2/\text{TaN}(001)$  surface compared with  $\text{Pd}_4/\text{TaN}(001)$  and Pd(111), consistent with the enhanced catalytic activity and  $\text{CO}_2$  selectivity in the experiments. The results imply that TaN and Sn modifications improve the ethanol complete oxidation through the C—C cleavage and bring the higher selectivity of  $\text{CO}_2$  and total EOR activity, which is in agreement with the CV, LSV, EIS and in situ ATR-SEIRAS results.

Furthermore, based on that  $\text{CH}_3\text{CO}$  and CO are rather stable on three surfaces and the  $\text{CH}_3\text{COO}^-$  fragment is detected in the in situ ATR-SEIRAS results, we also calculate the energy barriers of the following reactions (Table S9),  $\text{CH}_3\text{CO} + \text{OH} = \text{CH}_3\text{COOH}$  and  $\text{CO} + \text{OH} = \text{COOH}$ . It can be found that  $\text{CH}_3$  and CO can easily react with OH on  $\text{Pd}_4/\text{TaN}(001)$  and  $\text{Pd}_4\text{-SnO}_2/\text{TaN}(001)$ , leading the partial oxidation of  $\text{CH}_3\text{CH}_2\text{OH}$  to  $\text{CH}_3\text{COOH}$  dominated. Compared with the adsorption energies of  $\text{CH}_3\text{CO}$  and CO, it can be found that they can be removed by the abundant OH species. Specially, the activation energies of two reactions are only 0.62 and 0.54 eV, lower than those on Pd(111) and  $\text{Pd}_4/\text{TaN}(001)$ , suggesting that Sn modification brings high tolerance to  $\text{CH}_3\text{CO}$  and CO and promotes the subsequent oxidation of the ethanol fragments. These DFT calculations results are in accordance with in situ ATR-SEIRAS observations.

### 3.5. Brief discussion

As shown in Fig. S13, it is noted that both the pristine TaN and Sn are inactive to alkaline EOR in the potential region of 0–1.4 V. The catalytic activity of the commercial Pd/C is relatively lower. However, the PdSn-TaN/C catalyst modified with TaN and Sn exhibits superior catalytic activity, 26.9 times that of the commercial Pd/C. The presented structure characterizations demonstrate that the mixture is not a simple stack. The DRIFTS and HRTEM results confirm the presence of low-coordinated Pd sites for PdSn-TaN/C, which has been reported to be active for the alcohol oxidation reaction [14]. HRTEM results also indicate that PdSn-TaN/C presents a core-shell like structure, which can contribute to the effective interfacial interaction. This point can be further confirmed by the generated electron transfer in XPS results. In addition, XPS results also indicate that the TaN modification brings the Ta—O—Pd bond formation on the Pd-TaN interface, whose efficiency is further proved by the good catalytic activity of Pd-TaN/C, almost 22.4 times that of the commercial Pd/C. At the same time, as an oxyphilic metal, Sn modification can provide more non-lattice oxygen (i.g. OH) in the reaction process, and also brings a strengthened electronic interaction between PdSn and TaN. Overall, the excellent alkaline EOR activity of PdSn-TaN/C confirms that its unique geometric and electronic



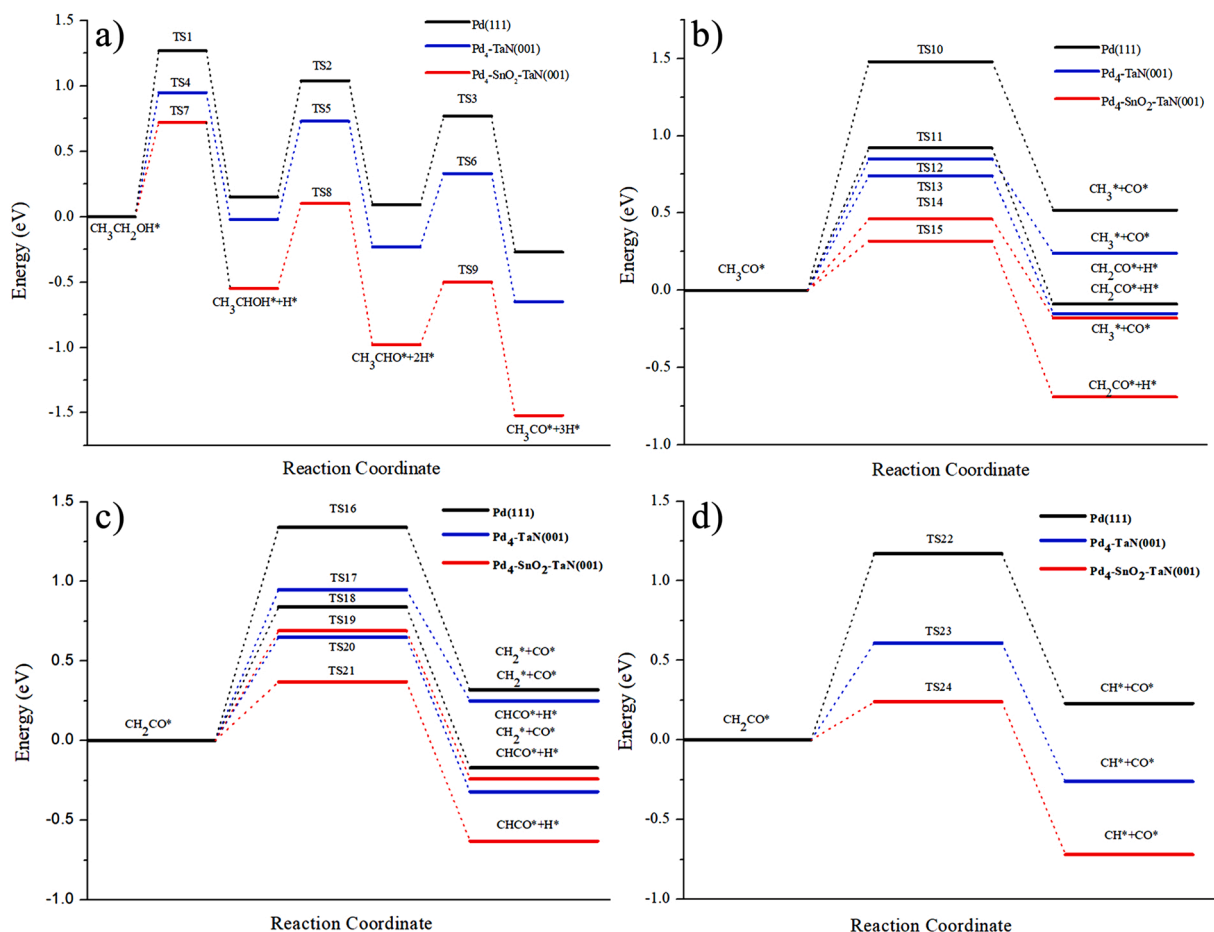


**Fig. 8.** (a) The potential energy profiles of CH<sub>3</sub>CH<sub>2</sub>OH<sub>ad</sub> oxidation to CH<sub>3</sub>CO<sub>ad</sub> on the Pd(111), Pd<sub>4</sub>/TaN(001) and Pd<sub>4</sub>-SnO<sub>2</sub>/TaN(001) surfaces; (b) The energy profiles of the C—C and C—H bonds cleavage for CH<sub>3</sub>CO on the Pd(111), Pd<sub>4</sub>/TaN(001) and Pd<sub>4</sub>-SnO<sub>2</sub>/TaN(001) surfaces. (c) The energy profiles of the C—C and C—H bonds cleavage for CH<sub>2</sub>CO on the Pd(111), Pd<sub>4</sub>/TaN(001) and Pd<sub>4</sub>-SnO<sub>2</sub>/TaN(001) surfaces. (d) The energy profiles of the C—C bond cleavage for CHCO on the Pd(111), Pd<sub>4</sub>/TaN(001) and Pd<sub>4</sub>-SnO<sub>2</sub>/TaN(001) surfaces.

structure on the PdSn-TaN/C interface is effective to catalyze ethanol dehydrogenation and oxidation in alkaline media.

Moreover, according to the presented electrochemical results, besides the outstanding catalytic activity, PdSn-TaN/C also exhibits the good catalytic durability among these catalysts, which can be ascribed to its good anti-CO ability. CO, an important intermediate, will poison the catalysts towards alkaline EOR because of its strong adsorption on the surface at lower potentials. To further gain insight into the promoting effects of TaN and Sn modification on the CO tolerance, CO stripping tests are carried out and shown in Fig. 9. It is found that the CO onset potentials of these catalysts follow the sequence of PdSn-TaN/C (0.67 V) < PdSn/C (0.69 V) < Pd-TaN/C (0.82 V) < Pd/C (0.89 V). The results demonstrate that both Sn and TaN contribute to the effective oxidation of CO, which is possibly because the easily generated OH can remove the adsorbed CO by the oxidation reaction to decrease the poisoning effect on the base of the bi-functional mechanism, in coincide with the DFT calculations and in situ ATR-SEIRAS results [27,39,112]. Specifically, on the one hand, the significantly negative shifts of the CO onset potentials after the presence of Sn suggest that Sn modification is favorable for the oxidation of CO. The OH formation appears to be sensitive to the presence of Sn with higher oxophilicity. This result is related to the amount increase of the surface non-lattice oxygen, which enhances the donation of the dangling OH by disturbing the interfacial H<sub>2</sub>O network, confirmed by XPS, CV and in situ ATR-SEIRAS results [9]. On the other hand, in this work, HRTEM, DRIFTD and XPS results further verify the unique structure of PdSn-TaN/C, that is, the low-coordinated Pd sites on the PdSn-TaN/C interface. It has been

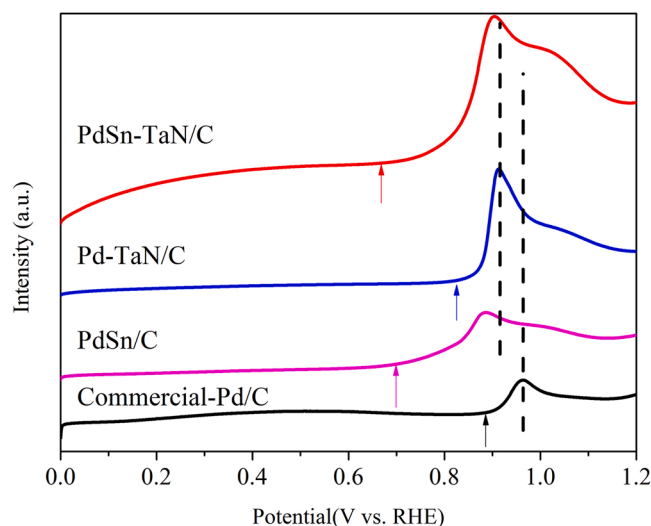


**Fig. 9.** The CO stripping voltammogram for the PdSn-TaN/C, Pd-TaN/C, PdSn/C and commercial Pd/C catalysts in Ar-saturated 0.5 M H<sub>2</sub>SO<sub>4</sub> solution at 20 mV/s (the arrows represent the onset potential of CO oxidation).

reported that the low-coordinated defect sites could provided the enhancement of the OH formation [77,84]. Besides, the OH<sup>-</sup> ions in alkaline medium are also sufficient to supply the non-adsorbed OH to



react with the CO by the above-mentioned E-L mechanism. Furthermore, due to the variance in electronic structures induced by the modification of TaN, the generated electron-deficient Pd will cause the negative-shift of the D-band center, thereby weakening the CO adsorption energy and accelerating the CO oxidation rate [32,69].

As for alkaline EOR, in addition to the mentioned activity and anti-CO poisoning ability, high selectivity of complete ethanol oxidation ( $\text{CO}_2$  selectivity) is also an important parameter to determine the EOR efficiency. The direct spectroscopic evidences provided by in situ ATR-SEIRAS results are shown to identify the reaction intermediates and understand the corresponding reaction mechanism. In particular, the respective roles of Sn and TaN are highlighted. For the commercial Pd/C, in situ ATR-SEIRAS results indicate that the incomplete ethanol electro-oxidation into acetate is predominant. It is found that a large amount of CO is adsorbed on Pd/C at lower potentials, indicating that the self-dissociation of ethanol is also active on the Pd surface. However, the oxidation removal of strongly adsorbed CO species is hindered for the commercial Pd/C due to the lack of OH, which results in its low selectivity of complete ethanol oxidation. For the PdSn-TaN catalysts, in situ ATR-SEIRAS results indicate that the C—C bonds splitting is favored on TaN-induced interface, whereas the subsequent oxidative removal process of intermediates (CO,  $\text{CH}_3\text{CO}$ ) by the generated OH preferentially occurs on the Sn sites, which is supported that the adsorption energies of them and the activation energies of  $\text{CH}_3\text{CO} + \text{OH} = \text{CH}_3\text{COOH}$  and  $\text{CO} + \text{OH} = \text{COOH}$  are weakened from DFT calculations. DFT results suggest that the activation energies of the C-H bond cleavage in  $\text{CH}_3\text{CH}_2\text{OH}$ ,  $\text{CH}_3\text{CHOH}$ ,  $\text{CH}_3\text{CHO}$ ,  $\text{CH}_3\text{CO}$  and  $\text{CH}_2\text{CO}$  and the C—C bond cleavage in  $\text{CH}_3\text{CO}$ ,  $\text{CH}_2\text{CO}$  and  $\text{CHCO}$  are reduced on the Pd<sub>4</sub>SnO<sub>2</sub>/TaN(001) surface, lower than those on Pd(111) and Pd<sub>4</sub>/TaN(001). It is indicated that TaN and Sn modification bring the higher selectivity of  $\text{CO}_2$  and total EOR activity, in agreement with the CV, LSV, EIS and in situ ATR-SEIRAS results.

Combining the above structure characterization, we can conclude that the presented electron transfer and Ta-O-Pd bond on the PdSn-TaN/C interface may contribute to the decrease of the barrier for the cleavage of C—C bonds to  $\text{CO}_2$ . Note that OH offered by Sn seems to only facilitate the subsequent oxidation of C1 fragments (i.g. CO) to enhance the anti-poisoning ability, but it is not active to the C—C bond cleavage. In summary, it can be indicated that a mixture of Sn and TaN on the Pd surface is required to optimize the catalytic activity of alkaline ethanol electro-oxidation, where TaN is responsible for the supply of effective interfacial active sites to split the C—C bonds, and Sn can provide oxygen functional groups to effectively enhance the intermediates oxidation kinetics. Those features enable PdSn-TaN/C to achieve a breakthrough for alkaline EOR with high ethanol utilization efficiency. The work provides guidelines for the design of high-efficiency TaN-based catalysts for alkaline ethanol electro-oxidation.

#### 4. Conclusions

This work reported the assembly of the PdSn-TaN/C catalyst via a facile solvothermal method. The rationally designed PdSn-TaN/C exhibited good catalytic activity ( $13025.84 \text{ A g}_{\text{Pd}}^{-1}$ ), durability and high  $\text{CO}_2$  selectivity to complete ethanol oxidation towards alkaline EOR. The outstanding catalytic performances of PdSn-TaN/C resulted from the construction of effective surface active sites. The HRTEM, and DRIFTS results confirmed the presence of the low-coordinated Pd sites on the PdSn-TaN/C with a core-shell like structure. XPS and CV results further indicated the existence of interfacial interaction, that is, Sn modification brought more surface non-lattice oxygen and TaN modification provided more interfacial interactions by the generation of Ta—O—Pd bonds, which led to the high catalytic activity. In situ ATR-SEIRAS and CV results demonstrated that, compared with the Pd-TaN/C, PdSn/C and Pd/C catalysts, PdSn-TaN/C displayed the highest activity and selectivity for  $\text{CO}_2$  formation, suggesting that it favored the complete oxidation of ethanol in alkaline media. The complete oxidation of alkaline ethanol to

$\text{CO}_2$  initially included the C—C bond cleavage, following by the further oxidation of the intermediates into  $\text{CO}_2$ . Analyzing the structure-function relationship, it could be found that TaN was mainly responsible to facilitate the C—C bond cleavage, whereas Sn favored the formation of OH and thus promoted the further oxidation of ethanol fragments, which were supported by in situ ATR-SEIRAS, CV and CO stripping results. DFT calculations also indicate the activation barriers of the C—H bond cleavage in  $\text{CH}_3\text{CH}_2\text{OH}$ ,  $\text{CH}_3\text{CHOH}$ ,  $\text{CH}_3\text{CHO}$ ,  $\text{CH}_3\text{CO}$ ,  $\text{CH}_2\text{CO}$  and the C—C bond cleavage in  $\text{CH}_3\text{CO}$ ,  $\text{CH}_2\text{CO}$ ,  $\text{CHCO}$  are evidently reduced on the PdSn-TaN/C surface compared with Pd-TaN/C and Pd/C, confirming the enhanced catalytic activity and  $\text{CO}_2$  selectivity in the experiments. The tolerance for  $\text{CH}_3\text{CO}$ ,  $\text{CH}_2\text{CO}$ ,  $\text{CHCO}$  and CO is also enhanced with the presence of TaN and Sn. Consequently, the combination of PdSn with TaN could be considered a good choice to accelerate the complete oxidation of alkaline ethanol with high utilization efficiency. This work may offer an idea for the design and construction of the high-efficient and inexpensive TaN-based catalysts for direct liquid fuel cells.

#### CRedit authorship contribution statement

**Ye Na:** Conceptualization, Methodology, Software, Validation, Formal analysis, Investigation, Data curation, Writing – original draft, Visualization. **Zhao Pengcheng:** Resources, Software, Data curation, Formal analysis, Writing – review & editing. **Qi Xiaoying:** Writing – review & editing. **Sheng Wenchao:** Resources, Writing – review & editing, Supervision. **Jiang Zhao:** Conceptualization, Methodology, Software, Resources, Writing – review & editing, Supervision, Project administration, Funding acquisition. **Fang Tao:** Resources, Supervision, Project administration, Funding acquisition.

#### Declaration of competing interest

The authors declare that they have no known competing financial interests or personal relationships that could have appeared to influence the work reported in this paper.

#### Acknowledgements

This work was supported by the National Natural Science Foundation of China (22075225, 21706203, 22038011 and 220005236), China Postdoctoral Science Foundation (2020T130508, 2019M660258 and 2019M663731), Special Guidance Funds for the Construction of World-Class Universities (Disciplines) and Characteristic Development in Central Universities (PY3A076), Fundamental Research Funds for the Central Universities (cxtd2017004, xjj2018035 and xjh012020030 in Xi'an Jiaotong University), Shaanxi Creative Talents Promotion Plan-Technological Innovation Team (2019TD-039), research funding from Beilin District (GX2017), research funding from the Joint Laboratory of Xi'an Jiaotong Univ. and Shaanxi Coal Chemical Industry Technology Research Institute Co. Ltd. The authors would like to thank Dr. Jiao Li, Engineer Jiamei Liu and Engineer Yu Wang at Instrument Analysis Center of Xi'an Jiaotong University, who provided guidance of characterization.

#### Appendix A. Supporting information

Supplementary data associated with this article can be found in the online version at [doi:10.1016/j.apcatb.2022.121473](https://doi.org/10.1016/j.apcatb.2022.121473).

#### References

- [1] J.N. Tiwari, N.K. Dang, H.J. Park, et al., Remarkably enhanced catalytic activity by the synergistic effect of palladium single atoms and palladium-cobalt phosphide nanoparticles, *Nano Energy* 78 (2020), 105166.

- [2] H. Peng, J. Ren, Y. Wang, et al., One-stone, two birds: Alloying effect and surface defects induced by Pt on Cu<sub>2-x</sub>Se nanowires to boost C-C bond cleavage for electrocatalytic ethanol oxidation, *Nano Energy* 88 (2021), 106307.
- [3] S. Zhang, K. Liu, Z. Liu, et al., Highly strained Au-Ag-Pd alloy nanowires for boosted electrooxidation of biomass-derived alcohols, *Nano Lett.* 21 (2021) 1074.
- [4] E.A. Monyoncho, S.N. Steinmann, C. Michel, et al., Ethanol electro-oxidation on palladium revisited using polarization modulation infrared reflection absorption spectroscopy (pm-irras) and density functional theory (DFT): why is it difficult to break the C-C bond? *ACS Catal.* 6 (2016) 4894–4906.
- [5] Y. Guo, B. Li, S. Shen, et al., Potential-dependent mechanistic study of ethanol electro-oxidation on palladium, *ACS Appl. Mater. Inter.* 13 (2021) 16602–16610.
- [6] S. He, Y. Liu, H. Li, et al., Highly dispersed Mo sites on Pd nanosheets enable selective ethanol-to-acetate conversion, *ACS Appl. Mater. Inter.* 13 (2021) 13311–13318.
- [7] L. Xiao, G. Li, Z. Yang, et al., Engineering of amorphous PtO<sub>x</sub> interface on Pt/WO<sub>3</sub> nanosheets for ethanol oxidation electrocatalysis, *Adv. Funct. Mater.* 31 (2021), 2100982.
- [8] S.W.M.J.P.A. Christensen, An in situ FTIR spectroscopic study of the electrochemical oxidation of ethanol at a Pb-modified polycrystalline Pt electrode immersed in aqueous KOH, *PCCP* 15 (2013) 17268.
- [9] Y. Katayama, T. Okanishi, H. Muroyama, et al., Enhanced supply of hydroxyl species in CeO<sub>2</sub>-modified platinum catalyst studied by in situ ATR-FTIR spectroscopy, *ACS Catal.* 6 (2016) 2026–2034.
- [10] N. Erini, V. Beermann, M. Gocyla, et al., The effect of surface site ensembles on the activity and selectivity of ethanol electrooxidation by octahedral PtNiRh nanoparticles, *Angew. Chem. Int. Ed.* 56 (2017) 6533–6538.
- [11] Z. Liang, L. Song, S. Deng, et al., Direct 12-electron oxidation of ethanol on a ternary Au(core)-PtIr(Shell) electrocatalyst, *J. Am. Chem. Soc.* 141 (2019) 9629–9636.
- [12] C.V.S. Almeida, G. Tremiliosi-Filho, K.I.B. Eguluz, et al., Improved ethanol electro-oxidation at Ni@Pd/C and Ni@PdRh/C core-shell catalysts, *J. Catal.* 391 (2020) 175–189.
- [13] M. Farsadrooh, J. Torrero, L. Pascual, et al., Two-dimensional Pd-nanosheets as efficient electrocatalysts for ethanol electrooxidation. Evidences of the C-C scission at low potentials, *Appl. Catal., B.* 237 (2018) 866–875.
- [14] W. Wang, X. Zhang, Y. Zhang, et al., Edge enrichment of ultrathin 2D PdPtCu trimetallic nanostructures effectuates top-ranked ethanol electrooxidation, *Nano Lett.* 20 (2020) 5458–5464.
- [15] Q. Chang, S. Kattel, X. Li, et al., Enhancing C-C bond scission for efficient ethanol oxidation using PtIr nanocube electrocatalysts, *ACS Catal.* 9 (2019) 7618–7625.
- [16] W. Zhu, J. Ke, S. Wang, et al., Shaping single-crystalline trimetallic Pt-Pd-Rh nanocrystals toward high-efficiency C-C splitting of ethanol in conversion to CO<sub>2</sub>, *ACS Catal.* 5 (2015) 1995–2008.
- [17] F. Lyu, M. Cao, A. Mahsud, et al., Interfacial engineering of noble metals for electrocatalytic methanol and ethanol oxidation, *J. Mater. Chem. A.* 8 (2020) 15445–15457.
- [18] S. Luo, L. Zhang, Y. Liao, et al., A tensile-strained Pt-Rh single-atom alloy remarkably boosts ethanol oxidation, *Adv. Mater.* 33 (2021), 2008508.
- [19] W. Du, G. Yang, E. Wong, et al., Platinum-Tin oxide core-shell catalysts for efficient electro-oxidation of ethanol, *J. Am. Chem. Soc.* 136 (2014) 10862–10865.
- [20] L. Luo, C. Fu, X. Yan, et al., Promoting effects of Au submonolayer shells on structure-designed Cu-Pd/Ir nanospheres: greatly enhanced activity and durability for alkaline ethanol electro-oxidation, *ACS Appl. Mater. Inter.* 12 (2020) 25961–25971.
- [21] R. Rizo, A. Bergmann, J. Timoshenko, et al., Pt-Sn-Co nanocubes as highly active catalysts for ethanol electro-oxidation, *J. Catal.* 393 (2021) 247–258.
- [22] M. Wang, R. Ding, Y. Xiao, et al., CoP/RGO-Pd hybrids with heterointerfaces as highly active catalysts for ethanol electrooxidation, *ACS Appl. Mater. Inter.* 12 (2020) 28903–28914.
- [23] J. Zhang, J. Ye, Q. Fan, et al., Cyclic penta-twinned rhodium nanobranches as superior catalysts for ethanol electro-oxidation, *J. Am. Chem. Soc.* 140 (2018) 11232–11240.
- [24] S. Bai, Y. Xu, K. Cao, et al., Selective Ethanol Oxidation Reaction at the Rh-SnO<sub>2</sub> Interface, *Adv. Mater.* (2020), 2005767.
- [25] A. Kowal, M. Li, M. Shao, et al., Ternary Pt/Rh/SnO<sub>2</sub> electrocatalysts for oxidizing ethanol to CO<sub>2</sub>, *Nat. Mater.* 8 (2009) 325–330.
- [26] M. Li, D.A. Cullen, K. Sasaki, et al., Ternary electrocatalysts for oxidizing ethanol to carbon dioxide: making Ir capable of splitting C-C bond, *J. Am. Chem. Soc.* 135 (2012) 132–141.
- [27] X. Yang, Z. Liang, S. Chen, et al., A phosphorus-doped Ag@Pd catalyst for enhanced C-C bond cleavage during ethanol electrooxidation, *Small* 16 (2020), 2004727.
- [28] B. Zhang, T. Sheng, Y. Wang, et al., Platinum-cobalt bimetallic nanoparticles with Pt skin for electro-oxidation of ethanol, *ACS Catal.* 7 (2017) 892–895.
- [29] Y. He, P. Ma, S. Zhu, et al., Photo-induced performance enhancement of tantalum nitride for solar water oxidation, *Joule* 1 (2017) 831–842.
- [30] M. Xiao, Z. Wang, B. Luo, et al., Enhancing photocatalytic activity of tantalum nitride by rational suppression of bulk, interface and surface charge recombination, *Appl. Catal. B: Environ.* 246 (2019) 195–201.
- [31] L. Wang, B. Zhang, Q. Rui, Plasma-induced vacancy defects in oxygen evolution cocatalysts on Ta<sub>3</sub>N<sub>5</sub> photoanodes promoting solar water splitting, *ACS Catal.* 8 (2018) 10564–10572.
- [32] N. Ye, Y. Bai, Z. Jiang, et al., Design the PdCu/Ta<sub>3</sub>N<sub>5</sub> C electrocatalyst with core-shell structure having high efficiency for methanol and formic acid oxidation reactions, *Electrochim. Acta* 383 (2021), 138365.
- [33] Y. Liu, M. Wei, D. Raciti, et al., Electro-oxidation of ethanol using Pt<sub>3</sub>Sn alloy nanoparticles, *ACS Catal.* 8 (2018) 10931–10937.
- [34] J. Heyes, M. Dunwell, B. Xu, CO<sub>2</sub> reduction on Cu at low overpotentials with surface-enhanced in situ spectroscopy, *J. Phys. Chem. C* 120 (2016) 17334–17341.
- [35] H. Miyake, S. Ye, M. Osawa, Electroless deposition of gold thin films on silicon for surface-enhanced infrared spectroelectrochemistry, *Electrochem. Commun.* 4 (2002) 973–977.
- [36] S. Zhu, X. Qin, Y. Yao, et al., pH-dependent hydrogen and water binding energies on platinum surfaces as directly probed through surface-enhanced infrared absorption spectroscopy, *J. Am. Chem. Soc.* 142 (2020) 8748–8754.
- [37] J.P. Perdew, K. Burke, M. Ernzerhof, Generalized gradient approximation made simple, *Phys. Rev. Lett.* 77 (1996) 3865–3868.
- [38] H.J. Monkhorst, J.D. Pack, Special points for Brillouin-zone integrations, *Phys. Rev. B* 13 (1976) 5188–5192.
- [39] N. Ye, P.C. Zhao, X. Qi, et al., Understanding the high performance of PdSn-TaN (tantalum nitride)/C electrocatalysts for the methanol oxidation reaction: coupling nitrides and oxophilic elements, *J. Mater. Chem. A* 10 (2021) 266–287.
- [40] N. Ye, Z. Jiang, T. Fang, Probing the enhanced methanol electrooxidation mechanism by promoted CO tolerance on the Pd catalyst modified with TaN: A combined experimental and theoretical study, *Int. J. Hydrog. Energ.* 46 (2021) 37321–37332.
- [41] N. Ye, Z. Jiang, T. Fang, Assembling the PdCu/rGO catalysts for methanol oxidation reaction in alkaline media by tuning the electronic structure, *Electrochim. Acta* 352 (2020), 136473.
- [42] M. Xiao, B. Luo, M. Lyu, et al., Single-crystalline nanomesh tantalum nitride photocatalyst with improved hydrogen-evolving performance, *Adv. Energy Mater.* 8 (2018), 1701605.
- [43] X. Zhao, T. Gunji, T. Kaneko, et al., An integrated single-electrode method reveals the template roles of atomic steps: disturb interfacial water networks and thus affect the reactivity of electrocatalysts, *J. Am. Chem. Soc.* 141 (2019) 8516–8526.
- [44] X. Yang, F. Ling, X. Zi, et al., Low-coordinate step atoms via plasma-assisted calcinations to enhance electrochemical reduction of nitrogen to ammonia, *Small* 16 (2020), 2000421.
- [45] K. Yin, Y. Chao, F. Lv, et al., One nanometer PtIr nanowires as high-efficiency bifunctional catalysts for electrosynthesis of ethanol into high value-added multicarbon compound coupled with hydrogen production, *J. Am. Chem. Soc.* 143 (2021) 10822.
- [46] Z.Y. Zhou, Z.Z. Huang, D.J. Chen, et al., High-index faceted platinum nanocrystals supported on carbon black as highly efficient catalysts for ethanol electrooxidation, *Angew. Chem. Int. Ed.* 49 (2010) 411–414.
- [47] A. Khan, M. Goepel, J.C. Colmenares, et al., Chitosan-based N-doped carbon materials for electrocatalytic and photocatalytic applications, *ACS Sustain. Chem. Eng.* 8 (2020) 4708–4727.
- [48] Q. Wang, L. Chen, S. Guan, et al., Ultrathin and vacancy-rich CoAl-layered double hydroxide/graphite oxide catalysts: promotional effect of cobalt vacancies and oxygen vacancies in alcohol oxidation, *ACS Catal.* 8 (2018) 3104–3115.
- [49] J. Liu, J. Zhang, Nanointerface chemistry: lattice-mismatch-directed synthesis and application of hybrid nanocrystals, *Chem. Rev.* 120 (2020) 2123–2170.
- [50] F. Zhao, C. Li, Q. Yuan, et al., Trimetallic palladium-copper-cobalt alloy wavy nanowires improve ethanol electrooxidation in alkaline medium, *Nanoscale* 11 (2019) 19448–19454.
- [51] M. Wassner, M. Eckardt, C. Gebauer, et al., Synthesis and electrocatalytic performance of spherical core-shell tantalum (oxy)nitride/nitrided carbon composites in the oxygen reduction reaction, *Electrochim. Acta* 227 (2017) 367–381.
- [52] M. Yang, M. Shen, J. Wang, et al., Pd-supported interaction-defined selective redox activities in Pd-Ce<sub>0.7</sub>Zr<sub>0.3</sub>O<sub>2</sub>-Al<sub>2</sub>O<sub>3</sub> model three-way catalysts, *J. Phys. Chem. C* 113 (2009) 12778–12789.
- [53] K. Murata, Y. Mahara, J. Ohyama, et al., The metal-support interaction concerning the particle size effect of Pd/Al<sub>2</sub>O<sub>3</sub> on methane combustion, *Angew. Chem. Int. Ed.* 56 (2017) 15993–15997.
- [54] M.J. Kale, P. Christopher, Utilizing quantitative in situ FTIR spectroscopy to identify well-coordinated Pt atoms as the active site for CO oxidation on Al<sub>2</sub>O<sub>3</sub>-supported Pt catalysts, *ACS Catal.* 6 (2016) 5599–5609.
- [55] H. Tiznado, S. Fuentes, F. Zaera, Infrared study of CO adsorbed on Pd/Al<sub>2</sub>O<sub>3</sub>-ZrO<sub>2</sub>: effect of zirconia added by impregnation, *Langmuir* 20 (2004) 10490–10497.
- [56] T. Lear, R. Marshall, J. Antonio Lopez-Sanchez, et al., The application of infrared spectroscopy to probe the surface morphology of alumina-supported palladium catalysts, *The J. Chem. Phys.* 123 (2005), 174706.
- [57] E. Ozensoy, D.C. Meier, D.W. Goodman, Polarization modulation infrared reflection absorption spectroscopy at elevated pressures: CO adsorption on Pd (111) at atmospheric pressures, *J. Phys. Chem. B* 106 (2002) 9367–9371.
- [58] S. Lu, Z. Zhuang, Investigating the influences of the adsorbed species on catalytic activity for hydrogen oxidation reaction in alkaline electrolyte, *J. Am. Chem. Soc.* 139 (2017) 5156–5163.
- [59] J. Masud, M.T. Alam, Z. Awaludin, et al., Electrocatalytic oxidation of methanol at tantalum oxide-modified Pt electrodes, *J. Power Sources* 220 (2012) 399–404.
- [60] J.T. Klopogge, L.V. Duong, B.J. Wood, et al., XPS study of the major minerals in bauxite: gibbsite, bayerite and (pseudo-)boehmite, *J. Colloid Interf. Sci.* 296 (2006) 572–576.
- [61] Q. Zhang, Y. Leng, R. Xin, A comparative study of electrochemical deposition and biomimetic deposition of calcium phosphate on porous titanium, *Biomaterials* 26 (2005) 2857–2865.

- [62] W. Zhan, Q. He, X. Liu, et al., A sacrificial coating strategy toward enhancement of metal-support interaction for ultrastable Au nanocatalysts, *J. Am. Chem. Soc.* 138 (2016) 16130–16139.
- [63] Y. He, Z.S. Fishman, K.R. Yang, et al., Hydrophobic CuO nanosheets functionalized with organic adsorbates, *J. Am. Chem. Soc.* 140 (2018) 1824–1833.
- [64] M. Wagner, P. Lackner, S. Seiler, et al., Resolving the structure of a well-ordered hydroxyl overlayer on  $\text{In}_2\text{O}_3$  (111): nanomanipulation and theory, *ACS Nano* 11 (2017) 11531–11541.
- [65] Q. Li, B. Yang, H. Lin, et al., Surface-controlled mono/diselective ortho C–H bond activation, *J. Am. Chem. Soc.* 138 (2016) 2809–2814.
- [66] K. Rajeshwar, N.R. de Tacconi, Solution combustion synthesis of oxide semiconductors for solar energy conversion and environmental remediation, *Chem. Soc. Rev.* 38 (2009) 1984.
- [67] Z. Zhu, F. Liu, J. Fan, et al., C2 alcohol oxidation boosted by trimetallic PtPbBi hexagonal nanoplates, *ACS Appl. Mater. Inter.* 12 (2020) 52731–52740.
- [68] R. Jayarajan, R. Kumar, J. Gupta, et al., Fabrication of an amyloid fibril-palladium nanocomposite: a sustainable catalyst for C–H activation and the electrooxidation of ethanol, *J. Mater. Chem. A* 7 (2019) 4486–4493.
- [69] L.S.R. Silva, C.V.S. Almeida, C.T. Meneses, et al., AuPd/C core-shell and alloy nanoparticles with enhanced catalytic activity toward the electro-oxidation of ethanol in alkaline media, *Appl. Catal. B* 251 (2019) 313–325.
- [70] J. Guo, R. Huang, Y. Li, et al., Surface structure effects of high-index faceted Pd nanocrystals decorated by Au submonolayer in enhancing the catalytic activity for ethanol oxidation reaction, *J. Phys. Chem. C* 123 (2019) 23554–23562.
- [71] C.D. Silva, P.G. Corradini, V. Del Colle, et al., Pt/Rh/Pt and Pt/Ru/Pt multilayers for the electrochemical oxidation of methanol and ethanol, *Electrochim. Acta* 354 (2020), 136674.
- [72] W. Du, G. Yang, E. Wong, et al., Platinum-tin oxide core-shell catalysts for efficient electro-oxidation of ethanol, *J. Am. Chem. Soc.* 136 (2014) 10862–10865.
- [73] F. Gao, Y. Zhang, F. Ren, et al., Universal surfactant-free strategy for self-standing 3D Tremella-Like Pd–M (M = Ag, Pb, and Au) nanosheets for superior alcohols electrocatalysis, *Adv. Funct. Mater.* 30 (2020), 2000255.
- [74] R. Kodiyath, G.V. Ramesh, E. Koudelkova, et al., Promoted C–C bond cleavage over intermetallic TaPt<sub>3</sub> catalyst toward low-temperature energy extraction from ethanol, *Environ. Sci.* 8 (2015) 1685–1689.
- [75] F. Zhu, K. Tu, L. Huang, et al., High selectivity PtRh/RGO catalysts for ethanol electro-oxidation at low potentials: enhancing the efficiency of CO<sub>2</sub> from alcoholic groups, *Electrochim. Acta* 292 (2018) 208–216.
- [76] C.V.S. Almeida, D.S. Ferreira, H. Huang, et al., Highly active Pt<sub>3</sub>Rh/C nanoparticles towards ethanol electrooxidation. influence of the catalyst structure, *Appl. Catal. B* 254 (2019) 113–127.
- [77] E.S. Valério Neto, C.V.S. Almeida, A.E. Russell, et al., Realising the activity benefits of Pt preferential (111) surfaces for ethanol oxidation in a nanowire electrocatalyst, *Electrochim. Acta* 348 (2020), 136206.
- [78] J.L. Bott-Neto, T.S. Martins, S.A.S. Machado, et al., Electrocatalytic oxidation of methanol, ethanol, and glycerol on Ni(OH)<sub>2</sub> nanoparticles encapsulated with poly [Ni(salen)] film, *ACS Appl. Mater. Inter.* 11 (2019) 30810–30818.
- [79] M.C. Figueiredo, R.M. Arán-Ais, J.M. Feliu, et al., Pt catalysts modified with Bi: enhancement of the catalytic activity for alcohol oxidation in alkaline media, *J. Catal.* 312 (2014) 78–86.
- [80] W. Huang, X.Y. Ma, H. Wang, et al., Promoting effect of Ni(OH)<sub>2</sub> on palladium nanocrystals leads to greatly improved operation durability for electrocatalytic ethanol oxidation in alkaline solution, *Adv. Mater.* 29 (2017), 1703057.
- [81] S. Beyhan, K. Uosaki, J.M. Feliu, et al., Electrochemical and in situ FTIR studies of ethanol adsorption and oxidation on gold single crystal electrodes in alkaline media, *J. Electroanal. Chem.* 707 (2013) 89–94.
- [82] B. Zhang, W. Lai, T. Sheng, et al., Ordered platinum-bismuth intermetallic clusters with Pt-skin for a highly efficient electrochemical ethanol oxidation reaction, *J. Mater. Chem. A* 7 (2019) 5214–5220.
- [83] C. Zhu, B. Lan, R. Wei, et al., Potential-dependent selectivity of ethanol complete oxidation on Rh electrode in alkaline media: a synergistic study of electrochemical ATR-SEIRAS and IRAS, *ACS Catal.* 9 (2019) 4046–4053.
- [84] J. Torroero, M.A. Peña, M. Retuerto, et al., Infrared study of the electrooxidation of ethanol in alkaline electrolyte with Pt/C, PtRu/C and Pt<sub>3</sub>Sn, *Electrochim. Acta* 319 (2019) 312–322.
- [85] J. Zhang, J. Ye, Q. Fan, et al., Cyclic penta-twinned rhodium nanobranches as superior catalysts for ethanol electro-oxidation, *J. Am. Chem. Soc.* 140 (2018) 11232–11240.
- [86] Z. Zhou, Q. Wang, J. Lin, et al., In situ FTIR spectroscopic studies of electrooxidation of ethanol on Pd electrode in alkaline media, *Electrochim. Acta* 55 (2010) 7995–7999.
- [87] L. Lin, W. Sheng, S. Yao, et al., Pt/Mo<sub>2</sub>C/C–cp as a highly active and stable catalyst for ethanol electrooxidation, *J. Power Sources* 345 (2017) 182–189.
- [88] M. Li, A. Kowal, K. Sasaki, et al., Ethanol oxidation on the ternary Pt–Rh–SnO<sub>2</sub>/C electrocatalysts with varied Pt:Rh:Sn ratios, *Electrochim. Acta* 55 (2010) 4331–4338.
- [89] Y. Yang, J. Ren, Q. Li, et al., Electrocatalysis of ethanol on a Pd electrode in alkaline media: an in situ attenuated total reflection surface-enhanced infrared absorption spectroscopy study, *ACS Catal.* 4 (2014) 798–803.
- [90] J. Zhang, X. Qu, Y. Han, et al., Engineering PtRu bimetallic nanoparticles with adjustable alloying degree for methanol electrooxidation: enhanced catalytic performance, *Appl. Catal. B* 263 (2020), 118345.
- [91] D. Chen, Y.J. Tong, An in-situ electrochemical IR investigation of solution CO electro-oxidation on a polycrystalline Au surface in an alkaline electrolyte: Identification of active reaction intermediates, *J. Electroanal. Chem.* 800 (2017) 39–45.
- [92] Z. Zhou, N. Tian, Y. Chen, et al., In situ rapid-scan time-resolved microscope FTIR spectroelectrochemistry: study of the dynamic processes of methanol oxidation on a nanostructured Pt electrode, *J. Electroanal. Chem.* 573 (2004) 111–119.
- [93] W. Wang, X. Chen, X. Zhang, et al., Quaternary Pt-based ultrathin nanowires intensified by Rh enable highly active and robust electrocatalysts for methanol oxidation, *Nano Energy* 71 (2020), 104623.
- [94] P. Li, K. Liu, J. Ye, et al., Facilitating the C–C bond cleavage on sub-10 nm concavity-tunable Rh@Pt core-shell nanocubes for efficient ethanol electrooxidation, *J. Mater. Chem. A* 7 (2019) 17987–17994.
- [95] J.M. Léger, Preparation and activity of mono- or bi-metallic nanoparticles for electrocatalytic reactions, *Electrochim. Acta* 50 (2005) 3123–3129.
- [96] Y. Yang, J. Ren, H. Zhang, et al., Infrared spectroelectrochemical study of dissociation and oxidation of methanol at a palladium electrode in alkaline solution, *Langmuir* 29 (2013) 1709–1716.
- [97] J.E. Sulaiman, S. Zhu, Z. Xing, et al., Pt–Ni octahedra as electrocatalysts for the ethanol electro-oxidation reaction, *ACS Catal.* 7 (2017) 5134–5141.
- [98] J. Li, S.Z. Jilani, H. Lin, et al., Ternary CoPtAu nanoparticles as a general catalyst for highly efficient electro-oxidation of liquid fuels, *Angew. Chem. Int. Ed.* 58 (2019) 11527–11533.
- [99] M. Arenz, K.J.J. Mayrhofer, V. Stamenkovic, et al., The effect of the particle size on the kinetics of CO electrooxidation on high surface area Pt catalysts, *J. Am. Chem. Soc.* 127 (2005) 6819–6829.
- [100] Y. Zhou, Y. Chen, K. Jiang, et al., Probing the enhanced methanol electrooxidation mechanism on platinum-metal oxide catalyst, *Appl. Catal., B* 280 (2021), 119393.
- [101] Q. Nian, J. Wang, S. Liu, et al., Aqueous batteries operated at -50 °C, *Angew. Chem. Int. Ed.* 58 (2019) 16994–16999.
- [102] M. Watanabe, T. Sato, K. Kunimatsu, et al., Temperature dependence of co-adsorption of carbon monoxide and water on highly dispersed Pt/C and PtRu/C electrodes studied by in-situ ATR-FTIRAS, *Electrochim. Acta* 53 (2008) 6928–6937.
- [103] Y.G. Yan, Q.X. Li, S.J. Huo, et al., Ubiquitous strategy for probing ATR surface-enhanced infrared absorption at platinum group metal-electrolyte interfaces, *J. Phys. Chem. B* 109 (2005) 7900–7906.
- [104] Q. Xu, A. Berná, I.V. Pobelov, et al., ATR-SEIRAS study of CO adsorption and oxidation on Rh modified Au(111–25 nm) film electrodes in 0.1 M H<sub>2</sub>SO<sub>4</sub>, *Electrochim. Acta* 176 (2015) 1202–1213.
- [105] H. Hanawa, K. Kunimatsu, H. Uchida, et al., In situ ATR-FTIR study of bulk CO oxidation on a polycrystalline Pt electrode, *Electrochim. Acta* 54 (2009) 6276–6285.
- [106] C. Li, J. Le, Y. Wang, et al., In situ probing electrified interfacial water structures at atomically flat surfaces, *Nat. Mater.* 18 (2019) 697–701.
- [107] L.F. Shen, B.A. Lu, Y.Y. Li, et al., Interfacial structure of water as a new descriptor of the hydrogen evolution reaction, *Angew. Chem. Int. Ed.* 59 (2020) 22397–22402.
- [108] Q. Zhang, Y. Ma, Y. Lu, et al., Modulating electrolyte structure for ultralow temperature aqueous zinc batteries, *Nat. Commun.* 11 (2020).
- [109] D. Chen, A.M. Hofstead-Duffy, I. Park, et al., Identification of the most active sites and surface water species: a comparative study of CO and methanol oxidation reactions on core-shell M@Pt (M = Ru, Au) nanoparticles by in situ IR spectroscopy, *J. Phys. Chem. C* 115 (2011) 8735–8743.
- [110] M. Li, W. Guo, R. Jiang, et al., Decomposition of ethanol on Pd(111): a density functional theory study, *Langmuir* 26 (2010) 1879–1888.
- [111] P. Ferrin, D. Simonetti, S. Kandoi, et al., Modeling ethanol decomposition on transition metals: a combined application of scaling and brønsted-evans-polanyi relations, *J. Am. Chem. Soc.* 131 (2009) 5809–5815.
- [112] Z. Wu, B. Miao, E. Hopkins, et al., Poisonous species in complete ethanol oxidation reaction on palladium catalysts, *J. Phys. Chem. C* 123 (2019) 20853–20868.